A scale-dependent analysis of the barotropic vorticity budget in a global ocean simulation

Hemant Khatri[1,2*], Stephen M. Griffies[2,3], Benjamin A. Storer[4], Michele Buzzicotti[5], Hussein Aluie[4,6], Maike Sonnewald[2,3], Raphael Dussin[3], Andrew Shao[7]

[1]Department of Earth, Ocean and Ecological Sciences, University of Liverpool, UK
[2]Atmospheric and Oceanic Sciences Program, Princeton University, USA
[3]NOAA Geophysical Fluid Dynamics Laboratory, Princeton, USA
[4]Department of Mechanical Engineering, University of Rochester, USA
[5]Department of Physics and INFN, University of Rome Tor Vergata, Italy
[6]Laboratory for Laser Energetics, University of Rochester, USA
[7]Canadian Centre for Climate Modelling and Analysis, Victoria, British Columbia, Canada

Key Points:

- Relative magnitudes of barotropic vorticity budget terms display significant length-scale dependence.
- Bottom pressure torque and wind stress curl control the depth-integrated meridional flow at length scales larger than 1000 km.
- Nonlinear advection and bottom pressure torque dominate the barotropic vorticity budget at smaller length scales.

*111, Nicholson Building, University of Liverpool, Liverpool L3 5DA, UK

Corresponding author: Hemant Khatri, `hkhatri@liverpool.ac.uk`

Abstract

The climatological mean barotropic vorticity budget is analyzed to investigate the relative importance of surface wind stress, topography, planetary vorticity advection, and nonlinear advection in dynamical balances in a global ocean simulation. In addition to a pronounced regional variability in vorticity balances, the relative magnitudes of vorticity budget terms strongly depend on the length-scale of interest. To carry out a length-scale dependent vorticity analysis in different ocean basins, vorticity budget terms are spatially coarse-grained . At length-scales greater than 1000 km, the dynamics closely follow the Topographic-Sverdrup balance in which bottom pressure torque, surface wind stress curl and planetary vorticity advection terms are in balance. In contrast, when including all length-scales resolved by the model, bottom pressure torque and nonlinear advection terms dominate the vorticity budget (Topographic-Nonlinear balance), which suggests a prominent role of oceanic eddies, which are of $\mathcal{O}(10-100)$ km in size, and the associated bottom pressure anomalies in local vorticity balances at length-scales smaller than 1000 km. Overall, there is a transition from the Topographic-Nonlinear regime at scales smaller than 1000 km to the Topographic-Sverdrup regime at length-scales greater than 1000 km. These dynamical balances hold across all ocean basins; however, interpretations of the dominant vorticity balances depend on the level of spatial filtering or the effective model resolution. On the other hand, the contribution of bottom and lateral friction terms in the barotropic vorticity budget remains small and is significant only near sea-land boundaries, where bottom stress and horizontal viscous friction generally peak.

Plain Language Summary

Vorticity provides a measure of the local circulation of fluid flow. The analysis of physical processes contributing to ocean vorticity has proven fundamental to our understanding of how those processes drive ocean flows, ranging from large-scale ocean gyres to boundary currents such as the Gulf Stream, which is tens of km in size. Furthermore, a vorticity analysis can inform us about the relative importance of different physical processes in generating flow structures having different length scales. In the present work, we perform a length-scale dependent vorticity budget analysis using a coarse-graining method to remove signals finer than a fixed length scale. We coarse-grain the climatological mean vorticity budget terms over a range of length scales, and then compare the relative magnitudes to identify the dominant vorticity balances as a function of length scale. We find that the spatial structure of the meridional transport is mainly controlled by atmospheric winds, variations in ocean depth and the momentum transport by ocean currents. However, the relative magnitudes of these factors change drastically at different length scales. We conclude that physical interpretations of the primary vorticity balances are fundamentally dependent on the chosen length scale of the analysis.

1 Introduction

Vorticity budget analyses are quite effective for understanding how surface winds drive ocean motions at different length scales. In particular, the classical Stommel model of the wind-driven gyre has provided significant insight into the linear, steady state balance of ocean gyres driven by surface wind stress (Stommel, 1948; Munk, 1950),

$$\rho_o \, \beta \, V = \hat{\boldsymbol{z}} \cdot \left(\nabla \wedge \boldsymbol{\tau}_{\mathrm{s}} - \nabla \wedge \boldsymbol{\tau}_{\mathrm{b}} \right). \tag{1}$$

Equation (1) shows that, in the absence of bottom stress τ_b, the vertical component of the surface wind stress curl, $\hat{\boldsymbol{z}}\cdot(\nabla\wedge\boldsymbol{\tau}_{\mathrm{s}})$, balances a meridional flow (V is the vertically-integrated meridional velocity) through the $\beta-$effect (β is the meridional gradient of the planetary vorticity), which is commonly known as "Sverdrup balance" (Sverdrup, 1947). Also, the mass conservation condition requires a return meridional flow in the zonally integrated vorticity balance, which appears to be controlled by bottom friction stress, $\hat{\boldsymbol{z}}\cdot(\nabla\wedge\boldsymbol{\tau}_{\mathrm{b}})$. The Stommel model effectively explained the east-west asymmetry due to nonzero β and flow intensification at the western boundary in the gyre circulation. In a slight modification, Munk (1950) argued that the ocean flow does not reach the ocean bottom so that horizontal friction acts mainly along the western boundary; thus, permitting a return flow along the western boundary.

The Stommel and Munk models apply to a flat bottom ocean since neither model accounts for bathymetry. If we take the curl of depth-integrated momentum equations to derive a linear vorticity equation in the presence of a variable topography at $z = -H(x, y)$, the resulting vorticity equation has an additional term known as the bottom pressure torque (Holland, 1973; Hughes & De Cuevas, 2001),

$$\rho_o \, \beta \, V = \hat{\boldsymbol{z}} \cdot \left(\nabla \wedge \boldsymbol{\tau}_{\mathrm{s}} - \nabla \wedge \boldsymbol{\tau}_{\mathrm{b}} \right) + J(p_{\mathrm{b}}, H). \tag{2}$$

A nonzero bottom pressure torque, $J(p_{\mathrm{b}}, H) = \hat{\boldsymbol{z}} \cdot (\nabla p_{\mathrm{b}} \wedge \nabla H)$, arises due to varying bottom pressure along isobath contours, and the variations in bottom pressure, p_{b}, exert a nonzero torque on fluid lying over a variable topography (Jackson et al., 2006). In essence, equation (2) implies that the return flow along the western boundary can be balanced by bottom pressure torque, and western boundary currents can be perceived as being largely inviscid because friction is not required to explain a closed gyre circulation (Hughes, 2000; Hughes & De Cuevas, 2001). In general, ocean flow along barotropic potential vorticity isolines would naturally allow the formation of western boundary currents and gyre circulations (Kiss, 2004; Welander, 1968). In fact, Schoonover et al. (2016) carried out vorticity budget analysis in realistic simulations from three different ocean models and found that bottom pressure torque controls the Gulf Stream flow magnitude along the western boundary; thus, the Gulf Stream is indeed largely inviscid (also see Gula et al., 2015; Le Bras et al., 2019). The three-way balance among $\rho_o \beta V$ (meridional advection of planetary vorticity), bottom pressure torque, and surface wind stress curl is called "Topographic-Sverdrup balance" (Holland, 1967). Notably, from the perspective of energy conservation, friction is ultimately necessary for maintainingan energy equilibrium state in the presence of energy input by wind forcing since bottom pressure torque does not dissipate energy (Jackson et al., 2006). However, in the presence of realistic bottom pressure torques, the role of friction (either bottom or side friction) for establishing basin-scale gyre circulations is no longer fundamental within the vorticity budget framework.

Several works have shown that bottom pressure torque appears as a first-order term in the vorticity budget of the depth-integrated flow and is crucial for understanding the returning boundary flows in gyres (Hughes & De Cuevas, 2001; Le Bras et al., 2019; Lu & Stammer, 2004; Sonnewald et al., 2019; Yeager, 2015). However, there remains significant regional variability in the relative magnitudes of vorticity budget terms. For example, in the North Atlantic Ocean, wind stress curl tends to be more important in controlling the depth-integrated meridional flow in the subtropics (except along the western boundary), whereas bottom pressure torque balances $\rho_o \beta V$ in almost all of the subpolar basin (Le Bras et al., 2019; Sonnewald & Lguensat, 2021; Yeager, 2015). Global analyses from ocean state estimates and in situ observations also show that the Sverdrup-balance holds only in the tropics and subtropics (Gray & Riser, 2014; Thomas et al., 2014; Wunsch, 2011). These differences in the interpretation of regional vorticity balances are partly due to the choice of regional boundaries for vorticity budget integration (Sonnewald et al., 2023). For example, bottom pressure torque vanishes when integrated over any area enclosed by an isobath, and the planetary vorticity advection appears to be controlled by wind stress and bottom friction (Kiss, 2004; Stewart et al., 2021). On the other hand, when integrating the vorticity budget over closed streamlines or fixed latitudinal bands, bottom pressure torque appears as the leading-order term. (Hughes & De Cuevas, 2001; Stewart et al., 2021).

In addition to the regional variability, spatial resolution in an ocean model affects the interpretation of dominant vorticity balances. In general, Stommel-Munk-type vorticity balances (equations 1 and 2) apply to large-scale ocean flows (see section 5.3 in Pedlosky, 1987). Thomas et al. (2014) showed that a linear Sverdrup balance only holds at length scales greater than 5° in ocean models. At relatively small length scales, i.e., mesoscales, western boundary currents, and multiple jets, ocean eddies and the associated nonlinearities make a notable contribution to the vorticity budget. For example, the nonlinear advection term in the vorticity equation (see equation 3) can induce narrow and fast western boundary currents in the opposite direction to the wind-driven Sverdrup transport (Fofonoff, 1955). Using an eddy-resolving simulation of the North Atlantic Ocean, Le Corre et al. (2020) showed that bottom pressure torque and curl of nonlinear advection terms appear to be the largest vorticity budget terms. On the other hand, in relatively coarse non-eddy-resolving and eddy-permitting ocean simulations, the nonlinear advection term tends to have a relatively small contribution to the overall vorticity budget (Yeager, 2015), and the meridional flow is mainly controlled by bottom pressure torque and surface wind stress. These differences arise because high resolution models permit the use of lower horizontal viscosity coefficients and can better resolve narrow boundary currents and nonlinear processes than coarse-resolution models (Griffies & Hallberg, 2000). Thus, interpretations of vorticity analyses depend on the region of interest, as well as the length scale of interest.

Several model-based vorticity analyses have shown that the relative magnitudes of vorticity budget terms depend on the details of model spatial resolution and associated representation of bathymetry (e.g. Hughes & De Cuevas, 2001; Le Corre et al., 2020; Yeager, 2015). However, a quantitative comparison is not feasible because these studies used different ocean models that significantly differ in terms of numerical methods, sub-grid parameterizations, and other features, each of which can affect the magnitudes of the vorticity terms (Styles et al., 2022). The present study investigates the primary balances in the vorticity budget of the depth-integrated flow in an eddy-permitting global ocean simulation and quantifies the impacts of spatial resolution on dynamical balances. In addition to analyzing the regional variability in vorticity budget terms, we examine how the relative magnitudes of these terms change as a function of length scale, which is achieved by employing a coarse-graining technique (Buzzicotti et al., 2023; Storer et al., 2022). In particular, spatial maps of vorticity budget terms are examined at different coarse-graining length-scales to understand the relative contributions of different processes in controlling the magnitude of planetary vorticity advection. The methodology is described in section 2, and the results are in section 3. Conclusions and broader implications of this study are discussed in section 4.

We offer four appendices that detail the methods used to perform a vorticity budget analysis and coarse-grain terms in that budget. Appendix A presents the mathematical expressions for the vorticity of the depth-integrated flow; Appendix B details the budget terms saved online in MOM6 ocean model and how we then compute the vorticity terms offline; and Appendix C discusses the magnitudes of the vorticity budget terms. Finally, Appendix D compares results from the coarse-graining method to the spatial filtering algorithm of Grooms et al. (2021), revealing that the two approaches agree qualitatively.

2 Methodology

2.1 Theory of Vorticity Budget Analysis

We analyze the vorticity budget based on the depth-integrated Boussinesq-hydrostatic ocean primitive equations. Several studies have employed this vorticity budget approach to examine the role of surface wind stress, bottom pressure, and ocean eddies in governing the flow dynamics (e.g. Le Corre et al., 2020; Hughes & De Cuevas, 2001; Yeager, 2015), see Waldman and Giordani (2023) for a recent review. The complete vorticity budget of the depth-integrated flow can be written as (see Appendix A for derivation)

$$\beta V = \frac{J(p_{\mathrm{b}}, H)}{\rho_o} + \hat{\boldsymbol{z}} \cdot \left(\frac{\nabla \wedge \boldsymbol{\tau}_{\mathrm{s}}}{\rho_o} - \frac{\nabla \wedge \boldsymbol{\tau}_{\mathrm{b}}}{\rho_o} + \nabla \wedge \mathcal{A} + \nabla \wedge \mathcal{B} \right) - f \frac{Q_m}{\rho_o} + f\, \partial_t \eta - \hat{\boldsymbol{z}} \cdot (\nabla \wedge \mathcal{U}_t)\,, \quad (3)$$

where $\beta = \partial_y f$ is the meridional derivative of the Coriolis parameter, V is the vertically-integrated meridional velocity, $z = \eta$ is the ocean free surface height, $z = -H$ is ocean bottom, p_{b} is bottom pressure, $\nabla = \hat{\boldsymbol{x}}\, \partial_x + \hat{\boldsymbol{y}}\, \partial_y$ is the horizontal gradient operator, and $\rho_o = 1035$ kg m^{-3} is the Boussinesq reference density. $\boldsymbol{\tau}_{\mathrm{s}}$ and $\boldsymbol{\tau}_{\mathrm{b}}$ are surface wind stress and bottom friction stress vectors, respectively. $\mathcal{A}$ and $\mathcal{B}$ represent the vertically integrated velocity advection and horizontal viscous friction terms. Q_m is the downward mass flux on the ocean surface and $\mathcal{U}_t$ is the vertically integrated velocity tendency term. By assuming a steady state, $Q_m = 0$, linearity, and a flat bottom ocean, equation (3) readily reduces to the Munk-Stommel model of wind-driven gyre given by equation (1).

It is important to note that there are other ways to derive a two-dimensional vorticity equation, e.g., compute the curl of the depth-averaged velocity equations (Mertz & Wright, 1992), and the curl of the velocity equations at each depth level and then compute the vertical integral or mean. All these formulations are equally valid and can be used depending on the research problem at hand (these variations on vorticity budgets are reviewed in Waldman & Giordani, 2023). In this study, we only use the vorticity budget formulation in equation (3), which will be referred to as the "barotropic vorticity budget". We discuss our results in the context of previous studies that used the same formulation.

2.2 Diagnosing Vorticity Budget Terms in a Global Ocean Simulation

For the vorticity budget analysis, we employ output from the global ocean-sea ice model GFDL-OM4.0, which is constructed by coupling the Modular Ocean Model version 6 (MOM6)(Adcroft et al., 2019; Griffies et al., 2020) with the Sea Ice Simulator version 2 (SIS2). GFDL-OM4.0 configuration uses a Mercator-bipolar grid and has nominal 1/4° horizontal grid resolution, which permits mesoscale eddies especially in the lower latitudes, and uses a hybrid z^*-isopycnal vertical coordinate, which significantly reduces artificial numerical mixing and the associated biases (Adcroft et al., 2019; Tsujino et al., 2020). The bottom topography is represented by linear piecewise fits, the same as that used by other isopycnal layered models. This approach provides an accurate representation of bottom pressure torques in a manner similar to terrain following models. For the present work, GFDL-OM4.0 was forced using JRA55-do.v1.4 reanalysis product (Tsujino et al., 2018) following the Ocean Model Intercomparison Project protocol (Griffies et al., 2016; Tsujino et al., 2020). Surface wind stress is computed relative to the ocean velocity, and stress is computed between the ice-ocean when ice is present, with the ice experiencing the winds rather than the ocean. Bottom frictional stress is computed using a quadratic bottom drag with a dimensionless drag coefficient of 0.003 and a constant background 'tide' speed of 0.1 m s^{-1} and, for the horizontal friction, biharmonic viscosity is used. Further model configuration details are provided in Adcroft et al. (2019). The time-mean model output for 60 years (1958–2017) is used for the barotropic vorticity budget analysis.

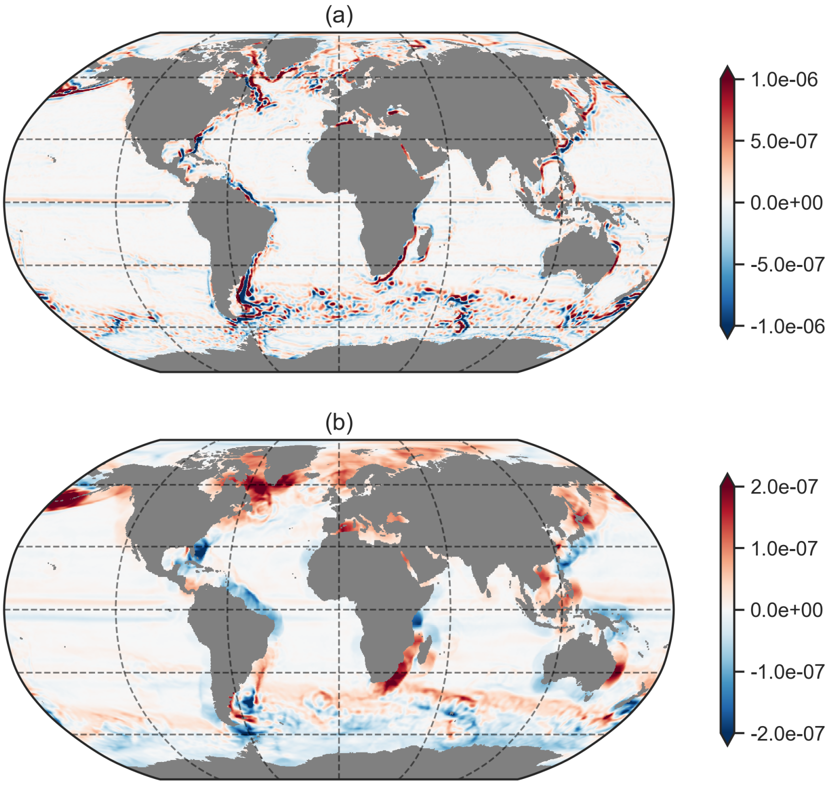

Figure 1. Spatial maps of the vertical component of relative vorticity (units are in s^{-1}) computed using the time-mean (1958–2017), depth-averaged velocity. The plotted vorticity maps are coarse-grained to (a) 200 km, (b) 1000 km horizontal length scale (using the FlowSieve package, Storer & Aluie, 2023). Note the different color ranges used for the two panels.

Since vorticity has a higher-order spatial derivative than velocity, the vorticity field can be very noisy due to strong spatial and regional variability, which is especially enhanced at small length scales (see the maps of relative vorticity of the depth-averaged flow in Figure 1). Hence, it requires additional care to have a fully closed barotropic vorticity budget. To diagnose the vorticity budget terms in equation (3), different terms in the depth-integrated primitive velocity equations from the model are saved as diagnostics, and the curl of these diagnostics is computed to obtain the relevant barotropic vorticity budget terms (see Appendix B for details). Computing the vorticity budget terms directly from the depth-integrals of velocity equation terms reduces numerical errors due to mathematical manipulations and interpolation, and the vorticity budget closes sufficiently for our purposes.

We point to the particularly difficult task of accurately computing bottom pressure torques using the Jacobian operator, $J(p_\mathrm{b}, H)$, which generally leads to significant numerical errors in regions of large topographic slopes. To minimize these numerical errors, bottom pressure torque can be computed as the residual of all other vorticity budget terms (Le Bras et al., 2019), or we can locally smooth bottom topography to obtain realistic magnitudes in bottom pressure torque (Le Corre et al., 2020). Our preferred method is to compute the curl of depth-integrated pressure gradient terms from the velocity equations. The same approach holds for the rest of the terms in the barotropic vorticity budget. Hence, to be consistent with the model numerical schemes and minimize the numerical errors in offline calculations, we compute vorticity budget terms directly from the depth-integrated momentum budget diagnostics, an approach used in many previous studies (Bell, 1999; Hughes & De Cuevas, 2001; Yeager, 2015). Since we calculate vorticity budget terms using the time-mean model output, our vorticity diagnostics include every modeled timescale and no Reynolds stress terms are required to close the vorticity budget (unlike the situation of offline calculation from time-mean prognostic fields). Note that, for calculating bottom pressure torque, we used the method described in Appendix B2 to minimize numerical errors.

As seen in the spatial maps of the time-mean vorticity budget terms (Figure 2a–2d), planetary vorticity advection, bottom pressure torque, the nonlinear advection curl, and the surface wind stress curl dominate the barotropic vorticity budget in terms of the magnitude. However, the vorticity balance tends to be very region dependent, as different terms dominate in different geographical locations (also see Sonnewald et al., 2019; Sonnewald & Lguensat, 2021). For example, bottom friction and lateral friction stress terms are relatively small in magnitude (Figure 2e–2f); however, these terms have notable contributions in local balances especially near continental boundaries. Similarly, we observe a drastic change in the relative magnitudes of vorticity budget terms and dominant vorticity balances as we vary the coarse-graining length scale. These characteristics of the vorticity budget terms motivate a length-scale-dependent vorticity analysis considered separately in different ocean regions (e.g. see Le Corre et al., 2020; Palóczy et al., 2020). Note that the remainder of the vorticity budget terms, which are associated with surface mass flux and time-tendencies (Figures 2g–2i), have a negligible contribution. Even so, we include them in the analyses to enable a fully closed vorticity budget.

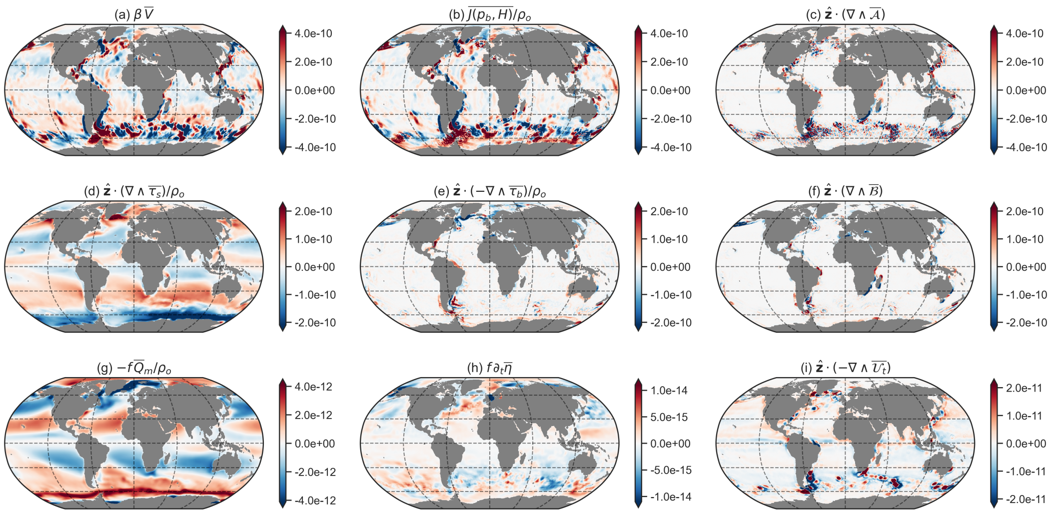

Figure 2. Time-mean (1958–2017, indicated with overbars) barotropic vorticity budget terms (units are in m s^{-2}). Each of the fields are coarse-grained to a 500 km length scale (used FlowSieve package, Storer & Aluie, 2023). Note the different colorbar ranges on the panels.

Signs of the barotropic vorticity budget terms can rapidly change spatially (e.g., see spatial variations in bottom pressure torque and nonlinear advection term in the Southern Ocean in Figures 2a–2c). Hence, positive and negative signals tend to cancel when integrated over large domains. For example, the global averages of bottom pressure torque and nonlinear advection vanish and the main balance is between surface wind stress and friction terms. As a result, a domain-averaged vorticity budget cannot pick up fields that have large magnitudes but with spatially alternating signs. Furthermore, the relative magnitudes of domain-averaged vorticity budget terms can be sensitive to the choice of domain boundaries (Sonnewald et al., 2023; Stewart et al., 2021). The resultant domain-averaged vorticity balance cannot represent the true nature of vorticity dynamics and can lead to incomplete or incorrect interpretations. To overcome these issues, we employ a coarse-graining technique to deduce the dominant vorticity budget terms appearing at different length scales (Buzzicotti et al., 2023). Coarse-graining allows us to examine the local and non-local impacts of different processes as a function of length scale, while maintaining the structure of the patterns corresponding to scales at or larger than the chosen coarse-graining scale. In the present work, we focus on the impacts of the choice of length scale on local barotropic vorticity balances.

2.3 The coarse-graining method

Coarse-graining can be used to examine the spatial variability in a multi-dimensional field. For any field, $F(\mathbf{x})$, the coarse-graining produces a filtered field, $F_\ell(\mathbf{x})$, that has variability on scales longer than ℓ, with variability on smaller scales preferentially removed (Buzzicotti et al., 2023). $F_\ell(\mathbf{x})$ is computed as

$$F_\ell(\mathbf{x}) = G_\ell * F(\mathbf{x}), \tag{4}$$

where $*$ is the convolution on the sphere (Aluie, 2019) and G_ℓ is a normalized filtering kernel, which is a top-hat filter in this study (see equation (4) in Storer et al., 2022), so that $\int_A G_\ell = 1$. Relation (4) basically represents a spatial average of $F(\mathbf{x})$ centered at geographical location $\mathbf{x}$.

In practice, the coarse-graining technique can be applied to the entire globe, which has land/sea boundaries, while preserving the fundamental physical properties, such as the global mean of a field and non-divergence of the velocity in a Boussinesq ocean (Aluie, 2019). Coarse-graining commutes with differential operators so that the coarse-grained equations resemble the original equations and the underlying mathematical properties of the system are preserved across different length scales. Coarse-graining has been successfully used for analyzing the kinetic energy spectrum and inter-scale energy transfers in the oceans (Aluie et al., 2018; Rai et al., 2021; Storer et al., 2022). Since the vorticity budget term magnitudes tend to peak around continental boundaries (Figure 2), spatial filtering near boundaries requires additional care so that there are no artificial large signals as a result of the spatial filtering. The coarse-graining technique is well suited for the present analysis as it handles gradients around land-sea boundaries appropriately (see details in Buzzicotti et al., 2023).

Following the steps described in section 2.2, we compute the barotropic vorticity budget diagnostics, which are then coarse-grained by employing the FlowSieve package (Storer & Aluie, 2023). Prior to coarse-graining, vorticity budget diagnostics were re-gridded from the native Mercator-bipolar grid (Adcroft et al., 2019) to a uniform $0.25^\circ \times 0.25^\circ$ grid using a conservative regridding method because the current implementation of FlowSieve package only accepts rectangular latitude-longitude grids. Since we only analyze the vertical vorticity component, the barotropic vorticity budget terms are treated as scalar fields for the purpose of coarse-graining. We use the fixed-kernel method, in which land is treated as ocean with a zero value of every vorticity balance term, to conserve global averages of vorticity terms (Buzzicotti et al., 2023). Coarse-grained diagnostics are then analyzed to identify the dominant vorticity balances as a function of coarse-graining scale, ℓ.

Furthermore, we compute the mean of the absolute values, $\{|F_\ell|\}$, for all the vorticity budget terms in different ocean regions and analyze their relative magnitudes as a function of coarse-graining scale,

$$\{|F_\ell|\} = \frac{\sum_i w_i |F_\ell(\mathbf{x_i})|}{\sum_i w_i}, \tag{5}$$

where i is a grid cell index within a region and w_i is the associated weight , equal to grid cell area on the uniform $0.25° \times 0.25°$ grid. The regional means of absolute values, $\{|F_\ell|\}$, are required to investigate the regional variability and length-scale-dependence in vorticity balances. If we instead preserve the signs of vorticity budget terms while calculating domain-averages, the positive and negative signals will offset each other, potentially resulting in incorrect interpretations of the dominant vorticity balances (see Figure 2). Note that $\{|F_\ell|\}$ magnitudes decline significantly with increasing the coarse-graining scale (see appendix Figure C1). Thus, we analyze the normalized $\{|F_\ell|\}$ magnitudes to measure the relative importance of different vorticity budget terms,

$$\{|F_\ell|\}_j\,\textit{(normalized)} = \frac{\{|F_\ell|\}_j}{\sum_j \left(\{|F_\ell|\}_j\right)}, \tag{6}$$

where j corresponds to a vorticity budget term and $\{|F_\ell|\}_j$ *(normalized)* measures the relative magnitude a vorticity budget term.

3 Vorticity Budget Analysis as a Function of Length-scale

Vorticity budget analyses from relatively coarse ocean models have shown that bottom pressure torque plays a prominent role in regional vorticity balances and in guiding western boundary currents (Hughes & De Cuevas, 2001; Lu & Stammer, 2004; Yeager, 2015; Zhang & Vallis, 2007). On the other hand, more recent studies employed mesoscale eddy-resolving ocean models having horizontal grid spacing of $2-10$ km, with these studies emphasizing that bottom pressure torque and nonlinear advection are equally important for regional vorticity dynamics (Le Corre et al., 2020; Palóczy et al., 2020). The present study aims to quantify the impacts of resolution on vorticity balances using a single global ocean simulation. Coarse-grained barotropic vorticity budget terms are examined as a function of coarse-graining scale in different ocean basins to assess the impact of spatial smoothing on the magnitudes of all vorticity terms.

3.1 Vorticity Budget in the North Atlantic Ocean

At first, we examine the spatial structure of coarse-grained vorticity budget terms in the North Atlantic Ocean, which has been considered in several works (e.g. Le Corre et al., 2020; Schoonover et al., 2016; Yeager, 2015; Zhang & Vallis, 2007). As seen in Figure 3, all vorticity terms, except the wind stress curl, have pronounced spatial variability and peak near continental boundaries and mid-ocean topographic features.

Coarse-graining has a notable impact on the relative contributions of different vorticity terms. For example, when spatial variations larger than 200 km are retained (Figures 3a1-3g1), planetary vorticity advection (βV), bottom pressure torque and the curl of the nonlinear advection term ($\nabla\wedge\mathcal{A}$), dominate in terms of the magnitude (also see Le Corre et al., 2020). Hence, the local meridional flow is controlled by bottom pressure torque and nonlinear advection (henceforth will be referred to as "Topographic-Nonlinear balance"). Surface wind stress, bottom friction, and horizontal friction terms also have large magnitudes around land-sea boundaries; however, their contribution to the local vorticity budget is relatively small. The rest of the vorticity budget terms (surface mass flux and time-tendencies) are negligible in comparison. There appears to be a significant cancellation between bottom pressure torque and $\nabla\wedge\mathcal{A}$ at mesoscales and submesoscales (smaller than about 500 km), and their sum is roughly in balance with βV. Our results are consistent with Le Corre et al. (2020), who found that bottom pressure torque and $\nabla\wedge\mathcal{A}$ signals generally are of opposite signs to each other, so that these two terms compensate for each other (also see Gula et al., 2015).

On the other hand, with coarse-graining at scales 1000 km and larger (Figures 3a3-3g3), the nonlinear advection term almost disappears, and the dominant balance is then among planetary vorticity advection, bottom pressure torque and wind stress curl. This result suggests that vorticity dynamics at large scales are close to the Topographic-Sverdrup balance, which agrees with vorticity budget analyses from relatively coarse ocean models (Lu & Stammer, 2004; Yeager, 2015). The coarse-graining exercise shows that bot-

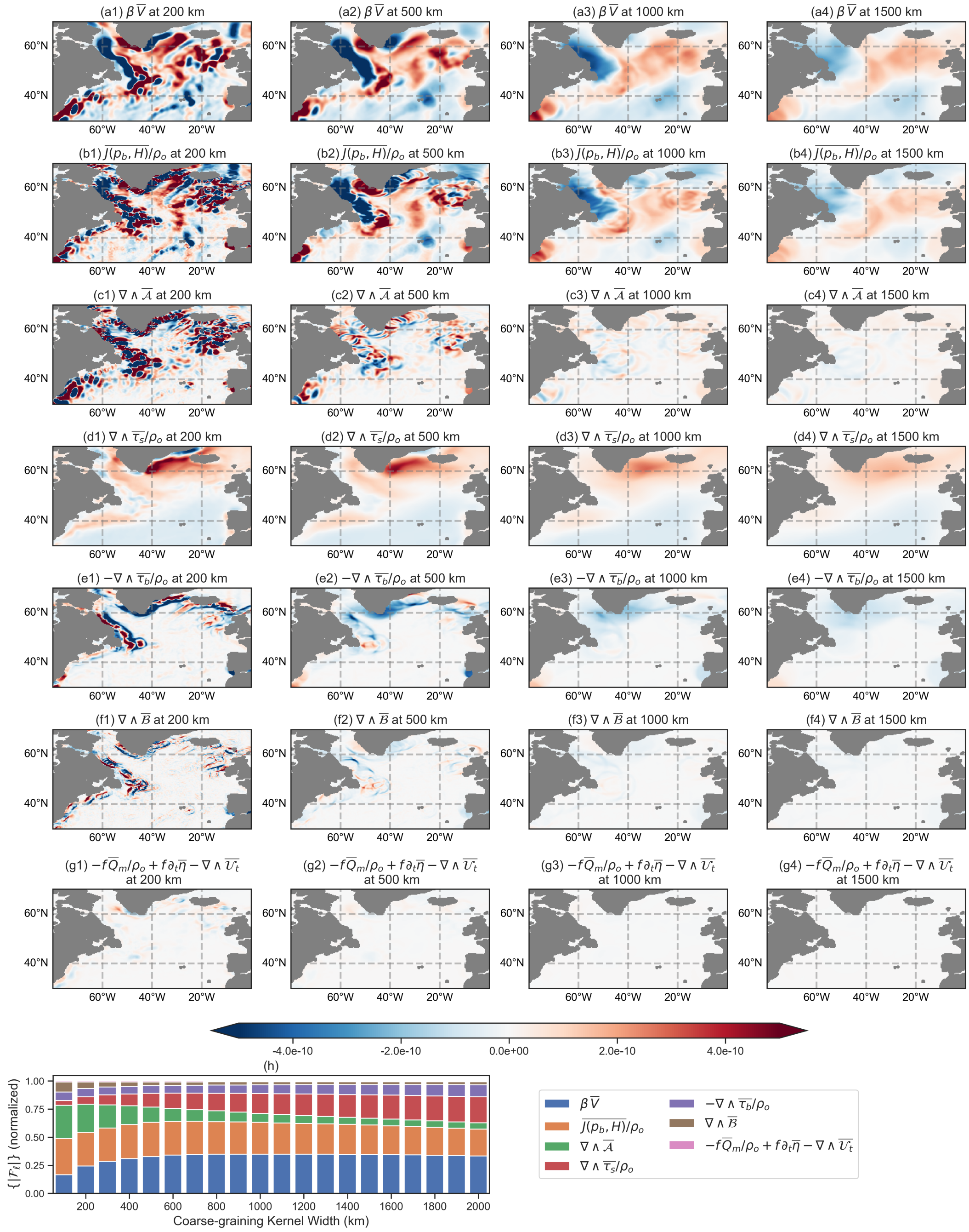

Figure 3. Vorticity budget analysis for the North Atlantic Ocean (a-g) Time-mean (1958–2017, indicated with overbars) spatial maps of barotropic vorticity budget terms (units are in m s^{-2}) as a function of the coarse-graining scale; (h) Normalized magnitudes of the absolute budget terms (see equation 6) at different coarse-graining scales . $\{|F_\ell|\}$ is computed for the region bounded between 30°N–70°N and 80°W–0°W. Note that $\hat{\boldsymbol{z}}\cdot$ is omitted in panel titles and legends.

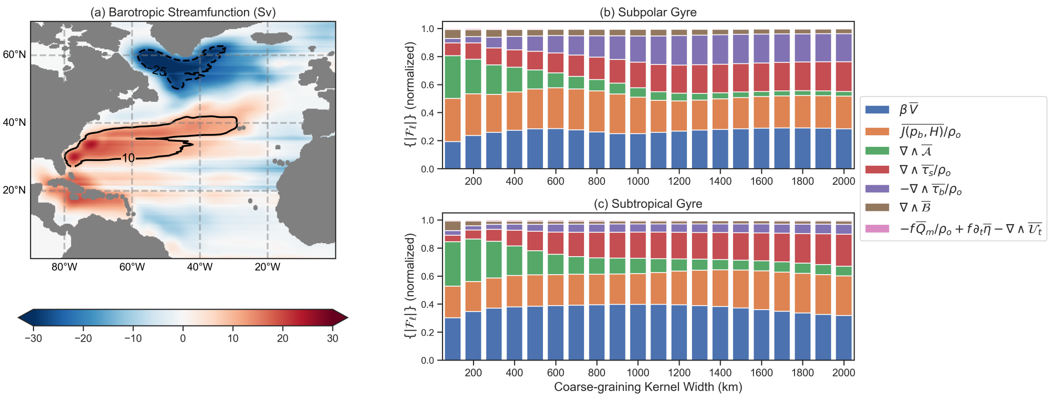

Figure 4. Vorticity budget analysis for for North Atlantic gyres (a) Time-mean (1958–2017, indicated with overbars) barotropic streamfunction computed as $\int_{x_w}^{x} \overline{V}\mathrm{d}x$; (b-c) Normalized magnitudes of the absolute budget terms (see equation 6) at different coarse-graining scales for the subpolar gyre (within the region of -25 Sv contour) and subtropical gyre (within the region of 10 Sv contour). The results are not sensitive to the choice of gyre contours, which were arbitrarily selected here. For brevity, $\hat{\boldsymbol{z}}\cdot$ is omitted in the legend.

tom pressure torque is significant at all length scales, whereas $\nabla\wedge\mathcal{A}$ contribution to the barotropic vorticity budget is limited to scales smaller than 1000 km. These results indicate that the model resolution (or the length scale of interest) is a key parameter while examining relative contributions from different vorticity terms, as physical interpretations of these results depend on the length scale.

For a quantitative investigation on the impacts of coarse-graining on vorticity balances, we compute normalized domain-averaged absolute values of the time-mean budget terms (Figure 3h). Consistent with the results discussed above, for coarse-graining with 200 km length scale (or smaller), bottom pressure torque and $\nabla\wedge\mathcal{A}$ are the largest in magnitude vorticity terms and represent more than 60% of the magnitudes of vorticity budget terms. βV is the third largest term and explains about 10% of the signals. As the coarse-graining kernel width increases, $\nabla \wedge \mathcal{A}$ signals smooth out, and the primary balance is then among βV, bottom pressure torque, and surface wind stress curl. Together, these three terms capture more than 70% of the vorticity budget at length scales greater than 1000 km. The rest of the contribution to the vorticity balance is from friction terms, $-\nabla \wedge \boldsymbol{\tau}_\mathrm{b}/\rho_o$ and $\nabla \wedge \mathcal{B}$, which project on all length scales. Overall, these vorticity analyses show a clear transition from the Topographic-Nonlinear balance to the

Topographic-Sverdrup balance as we move from small to large length-scales. The same results hold even if a different spatial filtering algorithm is used (see Figure D1).

3.1.1 Vorticity budget within closed gyre contours

To understand the dominant vorticity balances within subtropical and subpolar North Atlantic gyre circulations, we analyze $\{|F_\ell|\}$ magnitudes within closed gyre contours (Figure 4). Even within subtropical and subpolar gyres, the vorticity balance is largely among bottom pressure torque, $\nabla\wedge\mathcal{A}$, and βV when all length scales are included. When spatial features only larger than 1000 km are retained, there is a relatively small contribution from $\nabla \wedge \mathcal{A}$, and about 70% of the magnitudes of the barotropic vorticity terms are explained with βV, bottom pressure torque, and the surface wind stress curl. However, there is one key difference between the vorticity budgets of subtropical and subpolar gyres. At relatively large length-scales (greater than 500 km), bottom friction and horizontal friction terms, $-\nabla \wedge \boldsymbol{\tau}_\mathrm{b}/\rho_o$ and $\nabla \wedge \mathcal{B}$, capture about 20% of the signals in the subpolar gyre, whereas their contribution to the vorticity balance in the subtropical gyre is less than 10%. This difference is because a large part of the subpolar gyre is influenced by physical processes occurring near land-sea boundaries. Since bottom and horizontal friction have their peak magnitudes near continental boundaries (see Figures 3e–3f), they are more important in the vorticity budget of the subpolar gyre than in the subtropical gyre.

3.1.2 Why does the nonlinear advection term smooth out at large scales?

The nonlinear advection term mainly accounts for the redistribution of vorticity via western boundary currents, transient eddies and standing meanders (Gula et al., 2015), which generally are $1-300$ km in size (Chelton et al., 2007; Eden, 2007). Since these nonlinear flow patterns have spatial variations over length scales smaller than about 500 km, the nonlinear term is expected to be weak at large length scales (also see Hughes & De Cuevas, 2001). One can show that the nonlinear advection term has higher-order spatial derivatives than bottom pressure torque and βV (Appendix A2). This property indicates that the magnitude of the non-linear advection term decreases faster than other vorticity budget terms with increasing coarse-graining length scale. Therefore, at relatively large scales, bottom pressure torque, βV and wind stress curl are expected to be in balance (see Figures 3a1–3c1).

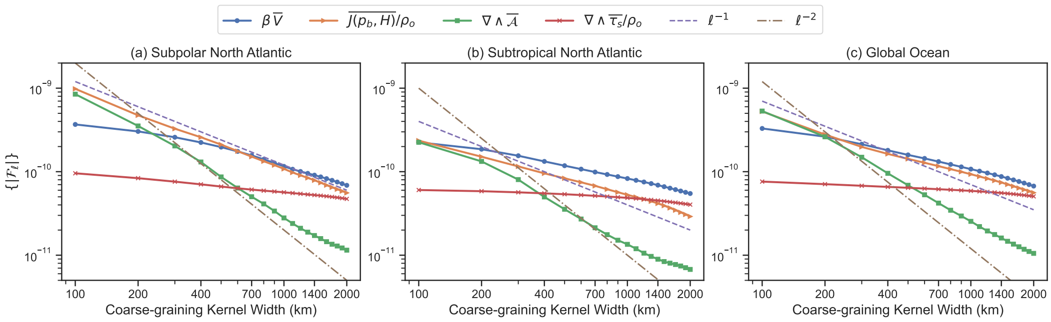

Figure 5. Scaling of the domain-mean magnitudes of vorticity budget terms, $|\{F_\ell\}|$ (units are in m s^{-2}), in (a) Subpolar North Atlantic Ocean (45°N–70°N and 80°W–0°W) (b) Subtropical North Atlantic (20°N–45°N and 80°W–0°W) (c) Global Ocean. Note that $\hat{\boldsymbol{z}}\cdot$ is omitted in the legends.

To further investigate the relative importance of the nonlinear advection term and bottom pressure torque at different length scales, we perform a scale analysis (also see Schoonover et al., 2016),

$$\left|\frac{J(p_\mathrm{b}, H)}{\rho_o}\right| = |\, f\, \mathbf{u}_g \cdot \nabla H\,| \quad \approx \quad f\,\frac{\mathcal{V}\mathcal{L}_v}{\mathcal{L}_h}, \tag{7}$$

$$|\,\hat{\boldsymbol{z}}\cdot(\nabla\wedge\mathcal{A})\,| \quad \approx \quad \frac{\mathcal{V}^2\mathcal{L}_v}{\mathcal{L}_h^2}, \tag{8}$$

where $\mathbf{u}_g$ is the horizontal geostrophic velocity at the ocean bottom, $\mathcal{V}$ is the velocity scale, $\mathcal{L}_h$ is the horizontal length scale, and $\mathcal{L}_v$ is the vertical length scale. Equations (7–8) imply that the magnitudes of bottom pressure torque and the nonlinear advection term follow $1/\mathcal{L}_h$ and $1/\mathcal{L}_h^2$ scalings, respectively. Hence, the nonlinear advection term must decay faster than bottom pressure torque when increasing the horizontal length scale. Therefore, at relatively large length scales, the meridional flow then has to be controlled by a combination of bottom pressure torque and surface wind stress. As seen in Figure 5, the domain-mean absolute values of the nonlinear advection term and bottom pressure torque (in both the subpolar North Atlantic and global ocean) are generally in agreement with these scaling arguments. However, in the subtropical North Atlantic, the decline seems to occur at a relatively slower pace. Overall, the nonlinear term roughly follows ℓ^{-2} scaling whereas the bottom pressure torque magnitude declines as ℓ^{-1}.

At relatively large scales, $\beta\,V$ dominates over $\nabla\wedge\mathcal{A}$ and the cross-over occurs near 200 km (Figure 5c), which interestingly corresponds to the mesoscale spectral peak in the global kinetic energy spectrum (Storer et al., 2022). Using the scale analysis, we estimate this cross-over length scale,

$$|\,\beta\, V\,| \quad \approx \quad |\,\hat{\boldsymbol{z}} \cdot (\nabla \wedge \mathcal{A})\,|\,, \tag{9}$$

$$\beta\,\mathcal{V}\mathcal{L}_v \quad \approx \quad \frac{\mathcal{V}^2\mathcal{L}_v}{\mathcal{L}_h^2}. \tag{10}$$

By setting $\beta = 10^{-11}$ m^{-1}s^{-1} and $\mathcal{V} = 0.1$ m s^{-1}, we obtain $\mathcal{L}_h = 100$ km, which largely agrees with the results from Figure 5. Thus, the contribution of the nonlinear advection term to the barotropic vorticity budget can be neglected at scales larger than 300–400 km, which was also argued by Hughes and De Cuevas (2001). Coincidentally, equation (10) implies a horizontal length scale of $\sqrt{\mathcal{V}/\beta}$, which is the same the inertial western boundary current scale proposed by (Fofonoff, 1955) and Rhines scale in geostrophic turbulence (Rhines, 1975). In a sense, all of these different theories predict a length scale beyond which linear flow dynamics takes over nonlinear eddy dynamics, thus the similarity in these different length scales is not surprising. Furthermore, many works have investigated the physical processes that determine these length scales over flat topography (Haidvogel et al., 1992; Ierley & Sheremet, 1995; Kiss, 2002).

One caveat to note is that our analyses use output from a 0.25° ocean model, which does not resolve all mesoscale activity. Hence, the contribution of the nonlinear advection term to barotropic vorticity budget, especially at mesoscales, is not fully captured. Furthermore, since we coarse-grain the barotropic vorticity budget terms diagnosed on the native model grid, coarse-graining does not remove Reynolds correlations arising from motions at length-scales smaller than the coarse-graining scale. Hence, if we were to calculate the nonlinear advection term in the barotropic vorticity budget using coarse-grained prognostic model diagnostics, such as velocities and layer thicknesses, as a function of coarse-graining scale, the length-scale dependence of $\nabla\wedge\mathcal{A}$ term may slightly differ from the one observed in Figure 5. Consequently, some results may not be directly compared against outputs from coarse non-eddy-resolving ocean models. On the other hand, $\beta\, V$ and bottom pressure torque terms are linear and do not suffer from issues related to nonlinear Reynolds stresses.

3.2 Vorticity Budget in Weddell Sea Region

Topography plays a fundamental role in the Southern Ocean, which comprises highly energetic ocean regions, e.g. Weddell Sea and Drake Passage, in terms of flow-topography interactions and mesoscale eddy dynamics (Hughes, 2005; Neme et al., 2023; Rintoul et

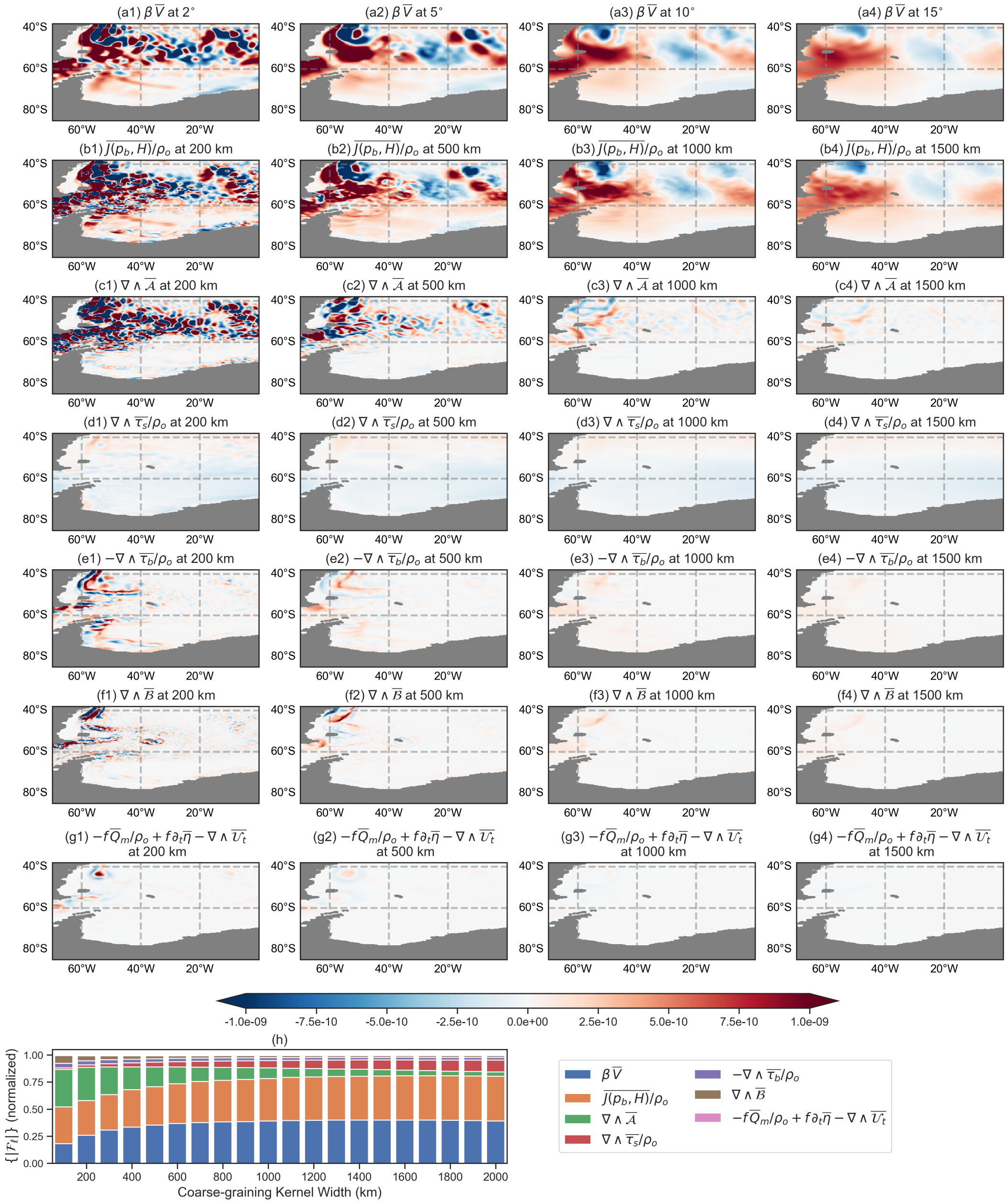

Figure 6. Vorticity budget analysis for the Weddell Sea region (a-g) Time-mean (1958–2017, indicated with overbar) spatial maps of barotropic vorticity budget terms (units are in m s^{-2}) as a function of the coarse-graining scale; (h) Normalized magnitudes of the absolute budget terms (see equation 6) at different coarse-graining scales . $\{|F_\ell|\}$ is computed for the region bounded between 85°S–40°S and 70°W–0°W. Note that $\hat{\boldsymbol{z}}\cdot$ is omitted in panel titles and legends.

al., 2001; Rintoul & Naveira Garabato, 2013; Rintoul, 2018). To investigate the roles of topography and nonlinear eddies on local vorticity balances, we repeat the vorticity budget analysis in the Weddell Sea region (Figure 6). For coarse-graining scale of 100–200 km, the main balance is among bottom pressure torque, $\nabla \wedge \mathcal{A}$, and βV. For coarse-grained fields at scales larger than about 1000 km, the contribution from the nonlinear advection term is minimal, and βV and bottom pressure torque terms explain more than 70% of the signals in the barotropic vorticity balances.

Interestingly, the relative contribution of the surface wind stress curl to the vorticity budget at length scales larger than 1000 km is much smaller than observed in the North Atlantic Ocean (compare Figures 3h and 6h). This behavior is because the magnitudes of βV and bottom pressure torque are much larger in the Southern Ocean than in the North Atlantic (Figures 2a–2b), whereas the wind stress curl magnitudes vary little with latitude (Figure 2d). In the Southern Ocean, the presence of prominent topographic features, in conjunction with substantial bottom pressure torque signals associated with strong bottom flows, gives rise to meandering and spatial variations in the flow structure due to topographic steering and potential vorticity conservation (Hughes, 2005; Kiss, 2004). As a consequence, the vorticity balance in this region prominently features substantial bottom pressure torque and βV signals, with wind stress curl playing a secondary role. These results do not imply that the wind component is unimportant in the Weddell Sea region. On the contrary, surface winds are a key driving force for ocean flows at all length scales. However, for the climatological local vorticity budget and spatial variability in vorticity terms, bottom pressure torque appears to be the primary factor in governing the spatial structure of the depth-integrated meridional flow in the Weddell Sea.

3.3 Vorticity Budget in the Equatorial Pacific Ocean

The equatorial Pacific Ocean slightly differs from ocean regions at high latitudes in terms of barotropic vorticity dynamics. Here, the contribution of the nonlinear advection term to the barotropic vorticity budget is relatively small at all length scales (Figure 7). Instead, bottom pressure torque and wind stress curl are the dominant terms that balance βV at all length scales, and these three terms capture more than 80% of the signals. Hence, dynamics in the equatorial Pacific Ocean largely follow the Topographic-Sverdrup balance. These results are in contrast to North Atlantic and Weddell Sea anal-

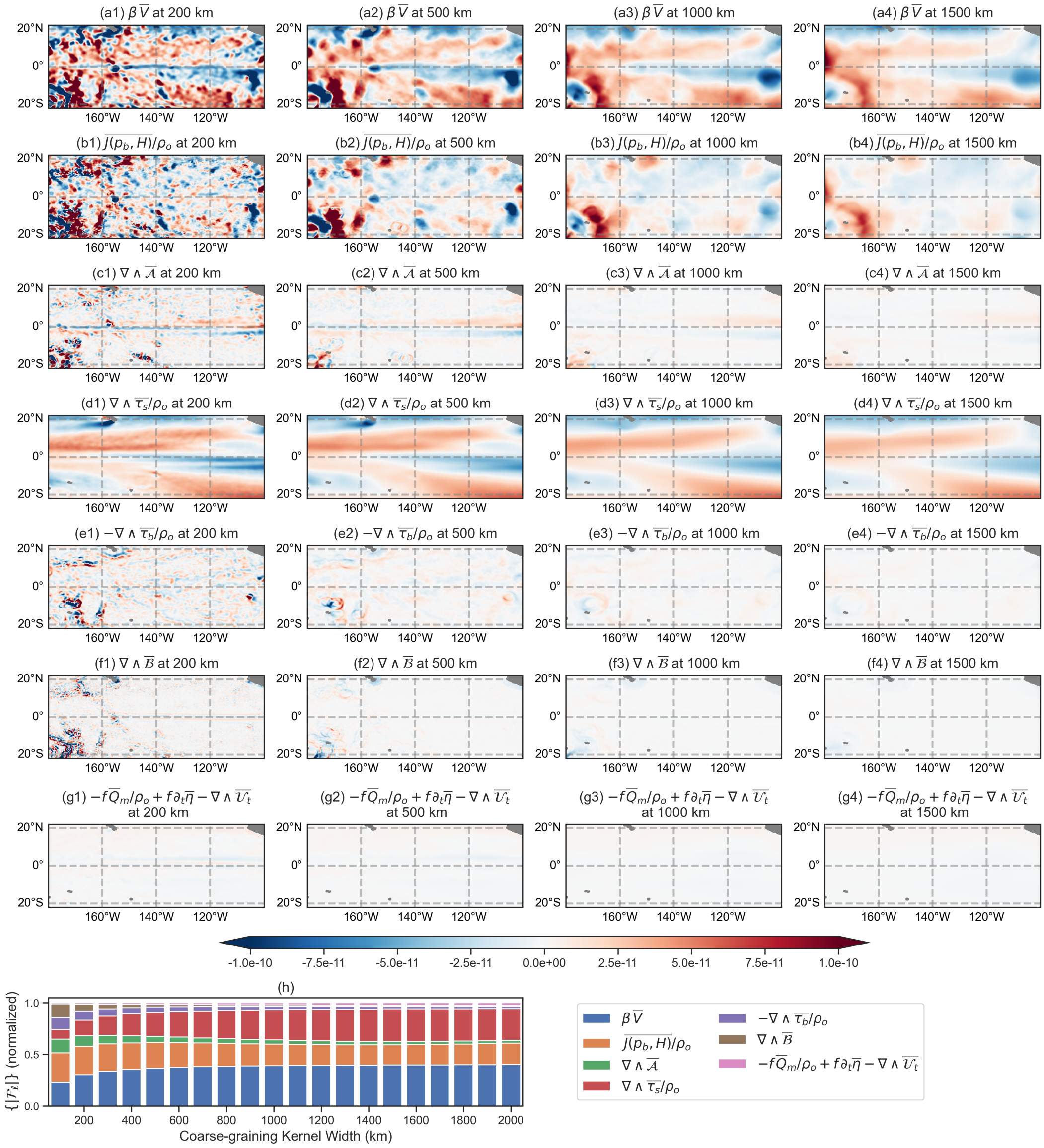

Figure 7. Vorticity budget analysis for an oceanic region in the equatorial Pacific (a-g) Time-mean (1958–2017, indicated with overbar) spatial maps of barotropic vorticity budget terms (units are in m s^{-2}) as a function of the coarse-graining scale; (h) Normalized magnitudes of the absolute budget terms (see equation 6) at different coarse-graining scales . $\{|F_\ell|\}$ is computed for the region bounded between 20°S–20°N and 180°W–100°W. Note that $\hat{\boldsymbol{z}}\cdot$ is omitted in panel titles and legends.

yses, which indicate significant nonlinear eddy advection contribution to vorticity dynamics at length scales smaller than 1000 km.

3.4 Global Vorticity Budget

To have an understanding of the global picture of vorticity balances, we divide the global ocean into four regions and repeat the vorticity analysis in these four regions (Figure 8). These basins are sufficiently large such that the regional variability (as in sections 3.1–3.3) becomes less apparent. In general, bottom pressure torque and βV terms are the largest terms, followed by the surface wind stress curl that appears on relatively large scales. These three terms together capture roughly 80% of the signals. As seen in sections 3.1–3.3, the nonlinear advection term is only important at length scales smaller than about 1000 km, except in the Indian Ocean sector where, even at length scales of 1000–2000 km, the nonlinear advection term is as important as surface wind stress curl and bottom pressure torque. The relatively large contribution of the nonlinear advection in the Indian Ocean could be due to larger mesoscale eddy length scales in tropics than at higher latitudes (Chelton et al., 2007, 2011). Similarly, we observe a relatively larger contribution of the nonlinear advection term in the Tropical Pacific-Atlantic region (Figure 8f). In addition, bottom friction and horizontal friction explain about 10%–20% of the signals in the vorticity balance in all four regions.

To further emphasize how spatial smoothing affects the local vorticity balance, we identify grid points at which 80% of the magnitudes in the barotropic vorticity budget can be explained with two or three largest vorticity terms. Sonnewald et al. (2019) applied a machine learning algorithm to ECCO global ocean state estimate, which has horizontal grid spacing of 1°, and identified different dynamical regimes using the barotropic vorticity budget framework. However, impacts of the spatial resolution on these dynamical regimes have not been examined before. Here, we analyze point-wise vorticity balances for four coarse-graining scales (Figure 9). Firstly, three vorticity balances stand out, i.e., Topographic-Sverdrup balance, Topographic-Nonlinear balance, and Sverdrup balance. The proportion of the global ocean surface area at which these balances are satisfied increases when we increase the coarse-graining scale (see Table 1). In fact, a large part of the global ocean transitions from a Topographic-Nonlinear regime to a Topographic-Sverdrup regime, especially in the Southern Ocean. As the coarse-graining kernel width increases and more length scales are filtered out, the contribution of the nonlinear ad-

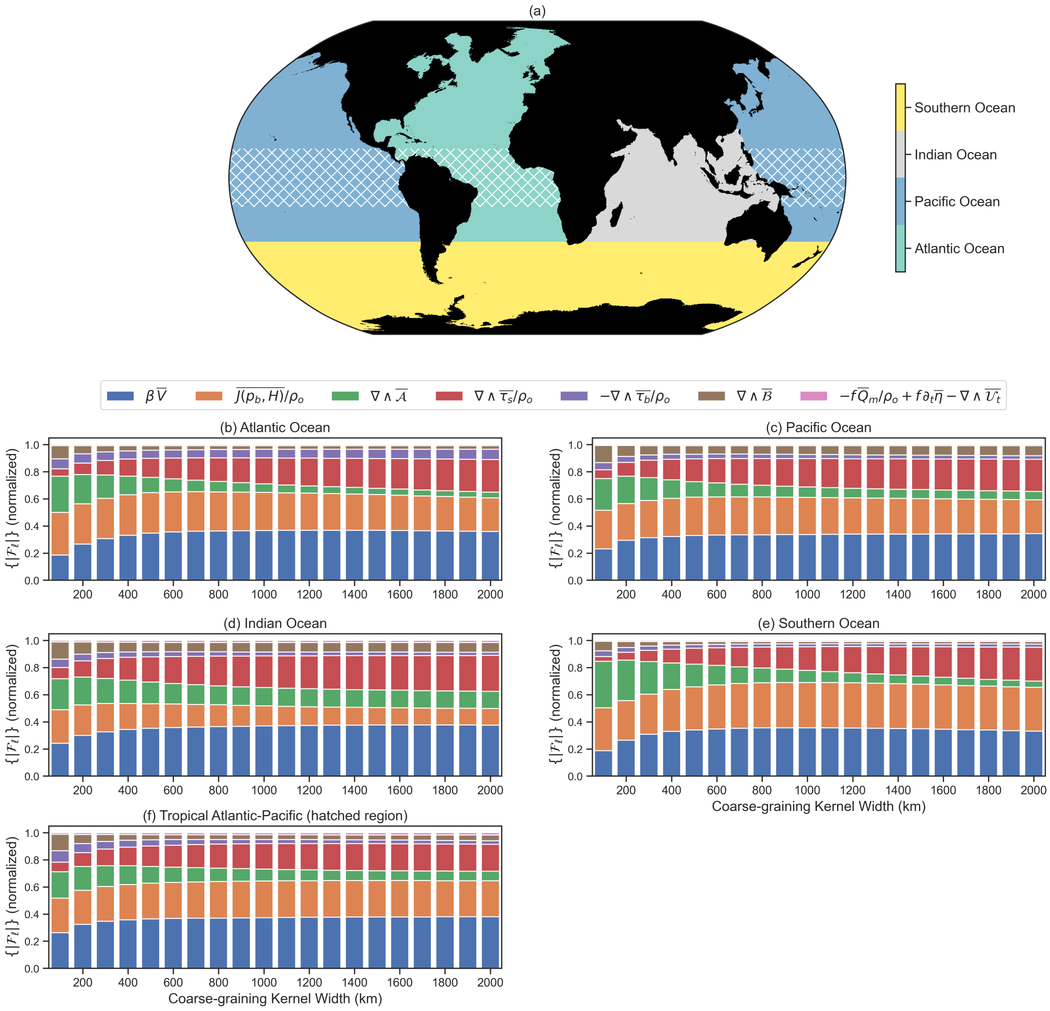

Figure 8. Vorticity budget analysis for the global ocean (a) Extent of four ocean basins (b-f) Normalized magnitudes of the absolute budget terms (see equation 6) at different coarse-graining scales . $\{|F_\ell|\}$ is computed separately for the basins shown with different colors in (a) and the hatched region covers tropical Atlantic-Pacific Ocean ($15°S - 15°N$). Note that $\hat{\boldsymbol{z}}\cdot$ is omitted in the legends.

vection term decreases. In the case of 200 km coarse-graining scale, the vorticity dynamics closely follow Topographic-Sverdrup and Topographic-nonlinear relationships at about 22% and 16% of the global ocean surface area, respectively. On the other hand, these percentages change to 37% and 6%, respectively, at length scales greater than 2000 km.

In tropical and subtropical oceans (roughly 40°S–40°N), Sverdrup balance holds reasonably well at length scales larger than 1000 km (Figure 9c), which is in agreement with Gray and Riser (2014); Thomas et al. (2014); Wunsch (2011). However, Sverdrup balance rarely holds at higher latitudes in those regions where topography significantly affects the spatial variability of the depth-integrated meridional flow at large scales. This role for topography is enhanced in such regions due to a relatively weak stratification allowing for strong deep flows. Note that maps of Sverdrup and Topographic-Sverdrup relationships in Figure 9 are not mutually exclusive. If the local vorticity dynamics can be approximated as being in Sverdrup balance (based on the chosen criteria of capturing 80% of the signals in the barotropic vorticity budget), then the dynamics would also be in accord with Topographic-Sverdrup balance. Hence , in the spatial maps shown in Figure 9, Sverdrup balance is a special case of Topographic-Sverdrup balance. At length scales larger than 1000 km, the barotropic vorticity dynamics can be understood in terms of Topographic-Sverdrup balance in more than 60% of the global ocean. A schematic of different dynamical regimes in the global ocean is shown in Figure 10.

Intriguingly, there is virtually no ocean region in the friction-dominated regime, in which planetary vorticity advection is controlled by bottom friction and horizontal friction. This result suggests that the global ocean is dominated by inviscid processes in terms of barotropic vorticity dynamics. Indeed, there is a large part of the oceans where these simplified vorticity relationships (Topographic-Nonlinear and Topographic-Sverdrup) do not hold and vorticity dynamics are controlled by more than three terms. In these regions, friction can play an important role, for example, by allowing flow across mean potential vorticity contours and altering western boundary current flow and separation (Hughes & De Cuevas, 2001; Jackson et al., 2006). In such situations, the combination of friction with other vorticity budget terms can alter the meridional transport structure and strength, leading to complex vorticity balances that may not be captured by simplified relationships shown in Figure 9. Additionally, Neme et al. (2023) identify the importance of bottom friction for transient vorticity budgets, thus offering a further caveat to the vorticity balances found here, which are based on climatological means (1958-2017).

4 Discussion and Conclusions

The vorticity budget of the depth-integrated flow is analyzed to understand how bottom pressure torque, surface wind stress curl, nonlinear advection, and friction drive spatial variability in meridional transport in the oceans. Previous studies have shown that interpretations of vorticity budget analyses can significantly change depending on the region of interest and length scale. For example, the classical Sverdrup balance only

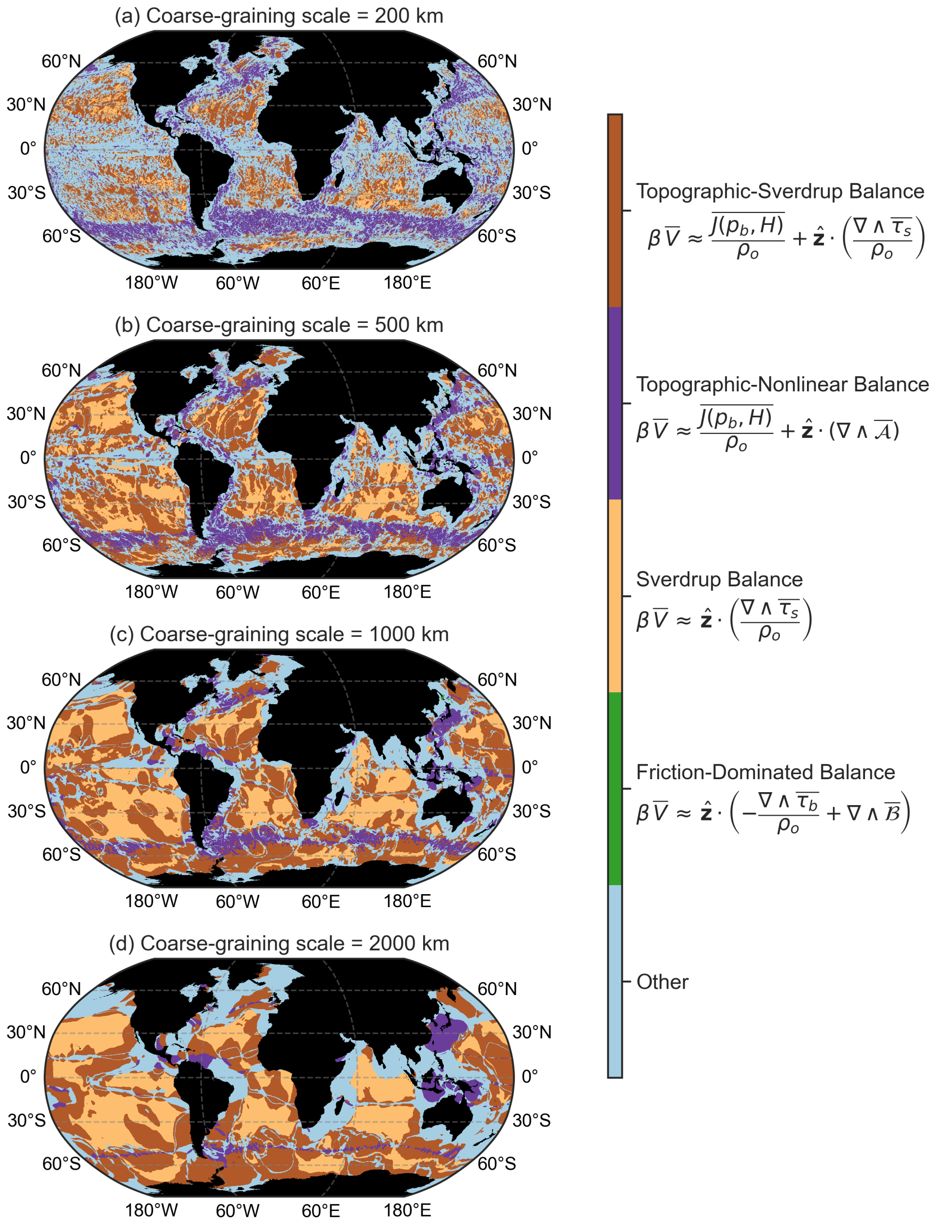

Figure 9. Global map of leading vorticity balances with different levels of coarse-graining (a) 200 km (b) 500 km (c) 1000 km (d) 2000 km. Different colors indicate balance among different vorticity terms (see legend), which capture 80% of the signals in the vorticity budget at any grid point. For legend 'Other', vorticity balance is complex, and more than three terms are required to capture 80% signals in vorticity balances.

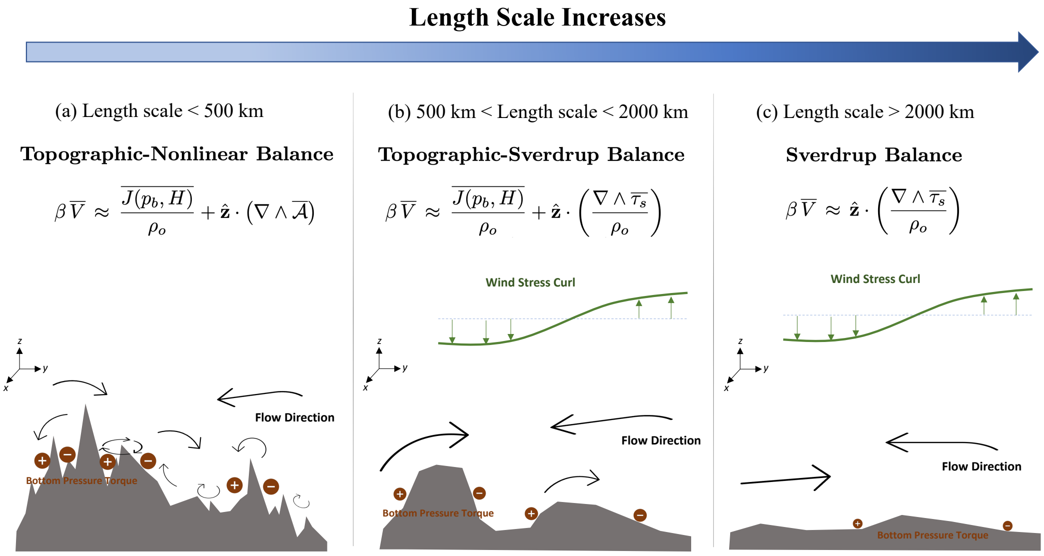

Figure 10. Schematic of primary barotropic vorticity balances and dynamical regimes as a function of length scale in a steady state. Both velocity field (see black arrows) and bottom pressure (brown $\pm$ circles) project on all length scales whereas surface wind stress projects only on large length scales. At length scales smaller than 500 km, nonlinear advection and bottom pressure torque control the spatial variability in meridional transport. At length scales greater than 500 km, meridional transport is mainly controlled by bottom pressure torque and surface wind stress curl as the nonlinear advection contribution is insignificant at large length scales.

	200 km	500 km	1000 km	2000 km
$\beta\,\overline{V} \;\approx\; \overline{J(p_{\rm b}, H)}/\rho_o + \hat{\boldsymbol{z}} \cdot (\nabla \wedge \overline{\boldsymbol{\tau}_{\rm s}})\,/\rho_o$	22.04%	34.73%	38.47%	37.00%
$\beta\,\overline{V} \;\approx\; \overline{J(p_{\rm b}, H)}/\rho_o + \hat{\boldsymbol{z}} \cdot (\nabla \wedge \overline{\mathcal{A}})$	16.14%	12.82%	9.16%	6.20%
$\beta\,\overline{V} \;\approx\; \hat{\boldsymbol{z}} \cdot (\nabla \wedge \overline{\boldsymbol{\tau}_{\rm s}})\,/\rho_o$	5.31%	16.22%	22.84%	27.04%
$\beta\,\overline{V} \;\approx\; \hat{\boldsymbol{z}} \cdot \left(-\nabla \wedge \overline{\boldsymbol{\tau}_{\rm b}}/\rho_o + \nabla \wedge \overline{\mathcal{B}}\right)$	0.15%	0.06%	0.06%	0.002%
Other	56.75%	39.03%	31.41%	30.85%

Table 1. Percentage of the global ocean surface area at which vorticity balances plotted in Figure 9 satisfy and capture more than 80% signals in vorticity balances.

holds in tropics and subtropics at length scales greater than about 5° (Thomas et al., 2014; Wunsch, 2011). At higher latitudes and in eddy-active regions, bottom pressure torque and nonlinear advection control the spatial variability in the depth-integrated meridional flow (Hughes & De Cuevas, 2001; Le Corre et al., 2020; Lu & Stammer, 2004; Yeager, 2015).

The present work investigates the regional variability and length-scale dependence in vorticity budget analyses using the 60-year mean vorticity budget terms from an eddy-permitting global ocean simulation (Adcroft et al., 2019). The time-mean vorticity budget terms are analyzed as a function of spatial-filtering scale by employing a coarse-graining technique (Buzzicotti et al., 2023; Storer et al., 2022). Consistent with previous studies (Hughes & De Cuevas, 2001; Sonnewald et al., 2019), the relative magnitudes of different vorticity budget terms display significant regional variability. In general, depth-integrated meridional velocity is balanced by a combination of the surface wind stress curl, bottom pressure torque, and the curl of the nonlinear velocity advection in the barotropic vorticity budget. The relative importance of these terms is examined by performing vorticity analyses in different ocean regions at different coarse-graining length scales.

We show that Topographic-Svedrup balance, in which $\beta\,V$ (meridional gradient of Coriolis parameter × depth-integrated meridional velocity), bottom pressure torque, and surface wind stress curl are in balance (Holland, 1967), applies to vorticity dynamics in the majority of the global ocean. These three vorticity terms capture more than 70% of the signals in the barotropic vorticity budget (Figures 3–8); however, it requires significant spatial coarse-graining, and this simplified balance only holds at length scales larger than about 1000 km. This result is in agreement with previous studies that employed coarse non-eddy resolving model outputs in their vorticity analyses (Lu & Stammer, 2004; Yeager, 2015). Although bottom pressure torque contribution is significant in all ocean regions that we considered, a simpler Sverdrup balance, in which the depth-integrated meridional transport is driven by surface wind stress curl (Sverdrup, 1947), holds reasonably well in subtropical oceans at length scales greater than 1000 km (also see Gray & Riser, 2014; Thomas et al., 2014; Wunsch, 2011). On the other hand, at higher latitudes and throughout the Southern Ocean, the contribution of bottom pressure torque for the vorticity balance cannot be neglected, with this importance due to relatively strong deep flows.

In the case of nominal or no coarse-graining (retaining variations on length scales greater than 100 km in the present work), bottom pressure torque and the nonlinear advection term dominate the vorticity budget locally (referred to as "Topographic-Nonlinear" balance here) indicating a prominent role of ocean eddies in vorticity balances. We note that bottom pressure torque and nonlinear advection terms compensate against each other (e.g. see Le Corre et al., 2020), and the residual from these two terms is roughly balanced by planetary vorticity advection. As we increase the length scale of coarse-graining, the nonlinear advection term largely smooths out, and we find a clear transition from Topographic-Nonlinear balance to Topographic-Sverdrup balance in the local vorticity budget (see Figure 9). Hence, the nonlinear advection term contributes to vorticity balances mostly at length scales smaller than 1000 km, and we offer a scaling argument to explain why it plays a negligible role for larger scale vorticity balances.

By incorporating the coarse-graining method in vorticity budget analysis, we find that the relative magnitudes of vorticity budget terms not only vary regionally but also have a strong length-scale dependence. Although Sverdrup and Topographic-Sverdrup relationships explain the spatial structure of the meridional transport in many places, these relationships only apply to large-scale oceanic flows (larger than about 1000 km). At relatively small length scales, the contribution of eddies and nonlinear advection to vorticity balance tends to be significant. Hence, the interpretations from vorticity analyses can be completely different depending on the extent of spatial filtering. We present a schematic describing these different vorticity balances (see Figure 10).

The present study only considers time-mean vorticity balances and the temporal variability in local vorticity balances has not been analyzed. Vorticity analyses from seasonal vorticity diagnostics (not shown) closely follow the time-mean results presented in the present work. In temporally varying vorticity diagnostics, we expect similar transitions among different dynamical regimes at different length scales (Figure 9) in barotropic vorticity balances, albeit some regional differences may be present. For example, although the contribution of the friction term is negligible in the time-mean vorticity balances, friction can play an important role in driving transient changes in vorticity balances (Neme et al., 2023).

Appendix A Vorticity Budget of the Depth-integrated Flow

The governing hydrostatic and Boussinesq ocean primitive velocity equation on a generalized vertical coordinate $r = r(x, y, z, t)$ is given by (Adcroft et al., 2019; Griffies et al., 2020)

$$\frac{\partial \mathbf{u}}{\partial t} + (f + \zeta)\,\hat{\boldsymbol{z}} \wedge \mathbf{u} + w^{(\dot{r})}\frac{\partial \mathbf{u}}{\partial r} = -\left[\frac{\nabla_r p}{\rho_o} + \nabla_r \Phi\right] - \nabla_r K + \mathcal{F} + \frac{\partial_r \tau}{\rho_o}, \tag{A1}$$

where we have

$\mathbf{v} = \mathbf{u} + \hat{\boldsymbol{z}}\,w = \hat{\boldsymbol{x}}\,u + \hat{\boldsymbol{y}}\,v + \hat{\mathbf{z}}\,w$	velocity	(A2)
$\nabla_r = \hat{\boldsymbol{x}}\left[\frac{\partial}{\partial x}\right]_r + \hat{\boldsymbol{y}}\left[\frac{\partial}{\partial y}\right]_r$	horizontal gradient on r-surface	(A3)
$w^{(\dot{r})} = \frac{\partial z}{\partial r}\frac{\mathrm{D}r}{\mathrm{D}t}$	dia-surface velocity used for remapping	(A4)
$\zeta = \left[\frac{\partial v}{\partial x}\right]_r - \left[\frac{\partial u}{\partial y}\right]_r$	r-coordinate vertical vorticity	(A5)
$-\left[\rho_o^{-1}\nabla_r p + \nabla_r \Phi\right]$	horizontal pressure acceleration ($\Phi = gz$)	(A6)
$K = \frac{u^2 + v^2}{2}$	horizontal kinetic energy per mass	(A7)
$\mathcal{F} = \mathcal{F}^{(\text{horz diff})} + \mathcal{F}^{(\text{vert diff})}$	horizontal and vertical diffusion	(A8)
$\partial_r \tau = \delta(z - \eta)\boldsymbol{\tau}_{\mathrm{s}} - \delta(z + H)\boldsymbol{\tau}_{\mathrm{b}}$	wind stress, $\boldsymbol{\tau}_{\mathrm{s}}$ and bottom drag, $\boldsymbol{\tau}_{\mathrm{b}}$	(A9)
$\delta(z)$	Dirac delta with dimensions L^{-1}	(A10)

A1 Depth integration and its curl

To derive the vorticity budget of the depth-integrated flow, we first vertically integrate the velocity equation (A1) from the ocean bottom, $z = -H(x, y)$, to the sea surface, $z = \eta(x, y, t)$),

$$\int_{-H}^{\eta} \partial_t \mathbf{u}\,\mathrm{d}z = -f\,\hat{\boldsymbol{z}} \wedge \int_{-H}^{\eta} \mathbf{u}\,\mathrm{d}z - \int_{-H}^{\eta} \left(\frac{\nabla_r p}{\rho_o} + \nabla_r \Phi\right) \mathrm{d}z + \frac{\boldsymbol{\tau}_{\mathrm{s}}}{\rho_o} - \frac{\boldsymbol{\tau}_{\mathrm{b}}}{\rho_o} + \int_{-H}^{\eta} \mathbf{a}\,\mathrm{d}z + \int_{-H}^{\eta} \mathbf{b}\,\mathrm{d}z. \tag{A11}$$

Here, $\mathbf{a} = -\zeta\,\hat{\boldsymbol{z}} \wedge \mathbf{u} - \nabla_r K - w^{(\dot{r})}\,\partial_r \mathbf{u}$ and $\mathbf{b} = \mathcal{F}^{(\text{horz diff})}$. Vertical integral of $\mathcal{F}^{(\text{vert diff})}$, which is the vertical convergence of the vertical viscous flux, with the viscous flux vanishing at the ocean top and bottom, over the whole depth vanishes. Since we use the depth-integrated velocity equation to derive the vorticity budget, the mathematical manipulations in the following steps remain the same irrespective of the choice of the vertical coordinate in the velocity equation. Thus, for simplicity, the pressure gradient term is just written as ∇p above (note that the geopotential, $\Phi = g\,z$, does not appear in horizontal pressure gradients), where $\nabla = \hat{\boldsymbol{x}}\,\partial_x + \hat{\boldsymbol{y}}\,\partial_y$ is the horizontal gradient operator on a fixed depth. We now introduce the shorthand notation

$$\mathcal{U}_t = \int_{-H}^{\eta} \partial_t \mathbf{u}\,\mathrm{d}z \quad \text{and} \quad \mathcal{A} = \int_{-H}^{\eta} \mathbf{a}\,\mathrm{d}z \quad \text{and} \quad \mathcal{B} = \int_{-H}^{\eta} \mathbf{b}\,\mathrm{d}z, \tag{A12}$$

and make use of Leibniz's rule on the pressure gradient term to render

$$\mathcal{U}_t = -f\,\hat{\boldsymbol{z}} \wedge \int_{-H}^{\eta} \mathbf{u}\,\mathrm{d}z - \frac{1}{\rho_o}\nabla\left[\int_{-H}^{\eta} p\,\mathrm{d}z\right] + p_s\,\nabla\eta + p_{\mathrm{b}}\,\nabla H + \frac{\boldsymbol{\tau}_{\mathrm{s}}}{\rho_o} - \frac{\boldsymbol{\tau}_{\mathrm{b}}}{\rho_o} + \mathcal{A} + \mathcal{B}. \tag{A13}$$

Here, p_{s} and p_{b} are pressures at the surface and bottom of the ocean, and the terms $p_{\mathrm{s}}\,\nabla\eta$, $p_{\mathrm{b}}\,\nabla H$ are pressure form stresses at the ocean surface and ocean bottom, respectively. We now take the curl of this equation and split the curl of the linear Coriolis term into two terms to obtain

$$\begin{aligned}
\nabla \wedge \mathcal{U}_t \quad &= \quad -\nabla \wedge \left(f\hat{\boldsymbol{z}} \wedge \int_{-H}^{\eta} \mathbf{u}\,\mathrm{d}z\right) - \frac{1}{\rho_o}\nabla \wedge \left(\nabla \int_{-H}^{\eta} p\,\mathrm{d}z - p_{\mathrm{s}}\,\nabla\eta - p_{\mathrm{b}}\,\nabla H\right) \\
&\quad + \frac{\nabla \wedge \boldsymbol{\tau}_{\mathrm{s}}}{\rho_o} - \frac{\nabla \wedge \boldsymbol{\tau}_{\mathrm{b}}}{\rho_o} + \nabla \wedge \mathcal{A} + \nabla \wedge \mathcal{B}, && \text{(A14)} \\
\hat{\boldsymbol{z}} \cdot (\nabla \wedge \mathcal{U}_t) \quad &= \quad -\beta \int_{-H}^{\eta} v\,\mathrm{d}z - f\,\nabla \cdot \int_{-H}^{\eta} \mathbf{u}\,\mathrm{d}z + \frac{J(p_{\mathrm{s}}, \eta)}{\rho_o} + \frac{J(p_{\mathrm{b}}, H)}{\rho_o} \\
&\quad + \hat{\boldsymbol{z}} \cdot \left(\frac{\nabla \wedge \boldsymbol{\tau}_{\mathrm{s}}}{\rho_o} - \frac{\nabla \wedge \boldsymbol{\tau}_{\mathrm{b}}}{\rho_o} + \nabla \wedge \mathcal{A} + \nabla \wedge \mathcal{B}\right). && \text{(A15)}
\end{aligned}$$

We can further manipulate the second term on the right hand side (RHS) by making use of volume conservation for a vertical column of Boussinesq fluid, which is

$$\nabla \cdot \int_{-H}^{\eta} \mathbf{u}\,\mathrm{d}z = \frac{Q_m}{\rho_o} - \partial_t \eta. \tag{A16}$$

In addition, ocean surface pressure is assumed to be constant, as is the case in the MOM6 configuration used here and often the case in climate models, so that $J(p_{\mathrm{s}}, \eta) =$

0. Finally, the vorticity budget for the depth-integrated flow (with some rearranging and writing $\int_{-H}^{\eta} v = V$) can be written as

$$\beta V = \frac{J(p_{\mathrm{b}}, H)}{\rho_o} + \hat{\boldsymbol{z}} \cdot \left(\frac{\nabla \wedge \boldsymbol{\tau}_{\mathrm{s}}}{\rho_o} - \frac{\nabla \wedge \boldsymbol{\tau}_{\mathrm{b}}}{\rho_o} + \nabla \wedge \mathcal{A} + \nabla \wedge \mathcal{B} \right) - f\, \frac{Q_m}{\rho_o} + f\, \partial_t \eta - \hat{\boldsymbol{z}} \cdot (\nabla \wedge \mathcal{U}_t)\,. \tag{A17}$$

A2 Manipulating the nonlinear advection term

$\nabla \wedge \mathcal{A}$ term can be further manipulated to represent it in a simpler form. In a $z-$coordinate model, we can write $\mathbf{a}$ as

$$\begin{aligned} \mathbf{a} &= a_x\, \hat{\boldsymbol{x}} + a_y\, \hat{\boldsymbol{y}} \qquad &(A18)\\ &= -\nabla_3 \cdot (\mathbf{v} u)\;\; \hat{\boldsymbol{x}} - \nabla_3 \cdot (\mathbf{v} v)\;\; \hat{\boldsymbol{y}}, \qquad &(A19)\end{aligned}$$

where $\mathbf{v} \;=\; \mathbf{u} + \hat{\boldsymbol{z}}\, w \;=\; \hat{\boldsymbol{x}}\, u + \hat{\boldsymbol{y}}\, v + \hat{\mathbf{z}}\, w$ is the velocity and $\nabla_3 \;=\; \nabla + \hat{\boldsymbol{z}}\, \partial_z$. We can integrate $\mathbf{a}$ vertically to obtain $\mathcal{A} = \mathcal{A}_x\, \hat{\boldsymbol{x}} + \mathcal{A}_y\, \hat{\boldsymbol{y}}$ (Leibniz's rule is also used),

$$\begin{aligned} \mathcal{A}_x &= a_x = -\int_{-H}^{\eta} \nabla_3 \cdot (\mathbf{v}\, u)\; \mathrm{d}z \qquad &(A20)\\ &= -\int_{-H}^{\eta} \nabla \cdot (\mathbf{u}\, u)\; \mathrm{d}z - [w\, u]^{z=\eta} + [w\, u]^{z=-H} \qquad &(A21)\\ &= -\nabla \cdot \int_{-H}^{\eta} (\mathbf{u}\, u)\; \mathrm{d}z + [\mathbf{u}\, u]^{z=\eta} \cdot \nabla \eta + [\mathbf{u}\, u]^{z=-H} \cdot \nabla H \\ &\quad - [w\, u]^{z=\eta} + [w\, u]^{z=-H}. \qquad &(A22)\end{aligned}$$

We can further simplify the above equation by using the surface and bottom kinematic boundary conditions,

$$\begin{aligned} \frac{\partial \eta}{\partial t} + \mathbf{u} \cdot \nabla \eta &= w + \frac{Q_m}{\rho_o} \quad \text{at} \quad z = \eta, \qquad &(A23)\\ -\mathbf{u} \cdot \nabla H &= w \quad \text{at} \quad z = -H. \qquad &(A24)\end{aligned}$$

Using equations (A22–A24) and following the same steps for A_y, we obtain

$$\begin{aligned} \mathcal{A}_x &= -\nabla \cdot \int_{-H}^{\eta} (\mathbf{u}\, u)\; \mathrm{d}z + \left(\frac{Q_m}{\rho_o} - \frac{\partial \eta}{\partial t} \right) [u]^{z=\eta} \qquad &(A25)\\ \mathcal{A}_y &= -\nabla \cdot \int_{-H}^{\eta} (\mathbf{u}\, v)\; \mathrm{d}z + \left(\frac{Q_m}{\rho_o} - \frac{\partial \eta}{\partial t} \right) [v]^{z=\eta} \qquad &(A26)\end{aligned}$$

Finally, the nonlinear advection term in the barotropic vorticity budget can be written

$$\begin{aligned} \nabla \wedge \mathcal{A} &= -\nabla \wedge \left(\hat{\boldsymbol{x}}\, \nabla \cdot \int_{-H}^{\eta} (\mathbf{u}\, u)\; \mathrm{d}z + \hat{\boldsymbol{y}}\, \nabla \cdot \int_{-H}^{\eta} (\mathbf{u}\, v)\; \mathrm{d}z \right) \\ &\quad + \nabla \wedge \left(\left(\frac{Q_m}{\rho_o} - \frac{\partial \eta}{\partial t} \right) [\mathbf{u}]^{z=\eta} \right), \qquad &(A27)\\ \nabla \wedge \mathcal{A} &= \frac{1}{\rho_o} \nabla \wedge \left(\nabla \cdot \int_{-H}^{\eta} \mathbb{T}^{\mathrm{kinetic}}_{\mathrm{hor}}\, \mathrm{d}z \right) + \nabla \wedge \left(\left(\frac{Q_m}{\rho_o} - \frac{\partial \eta}{\partial t} \right) [\mathbf{u}]^{z=\eta} \right), \qquad &(A28)\end{aligned}$$

where $\mathbb{T}_{\mathrm{hor}}^{\mathrm{kinetic}} = -\rho_o \, \mathbf{u} \otimes \mathbf{u}$ is the horizontal kinetic stress tensor. The second term of the RHS in equation (A28) is generally very small and can be neglected (Figure 2). Thus, the nonlinear advection term is mainly due to $\mathbb{T}_{\mathrm{hor}}^{\mathrm{kinetic}}$.

To better understand the relative importance of the nonlinear advection term in the barotropic vorticity balances, we examine the vorticity budget equation more closely. Since meridional transport is primarily controlled by bottom pressure torque and nonlinear advection at small length scales (Figures 3–4), an approximate vorticity budget can be written as

$$\beta V \approx \hat{\boldsymbol{z}} \cdot \left[\frac{1}{\rho_o} \nabla \wedge (H \, \nabla p_{\mathrm{b}}) + \overbrace{\frac{1}{\rho_o} \nabla \wedge \left(\nabla \cdot \int_{-H}^{\eta} \mathbb{T}_{\mathrm{hor}}^{\mathrm{kinetic}} \, \mathrm{d}z \right)}^{\approx \nabla \wedge \mathcal{A}} \right], \tag{A29}$$

Note that there are higher-order derivatives in the nonlinear advection term and bottom pressure torque. Hence, relative to βV, the right-hand side terms have a stronger small-scale spatial variability and relatively larger magnitudes at small length scales. As conjectured by Hughes (2000), the advection term and bottom pressure torque are expected to compensate each other at small length scales, with their residual leading to a relatively large-scale structure in meridional transport (see Figures 3a1–3c1).

Appendix B Diagnosing Vorticity Budget Terms in MOM6

MOM6 is equipped with online diagnostics sufficient for an offline computation of individual terms in the vorticity equations (A17). We do so by making use of the online depth-integrated velocity budget diagnostics in MOM6. We then take the curl of these diagnostics to obtain the corresponding vorticity budget terms. Actual names of depth-integrated momentum diagnostics and the relevant calculations are shown in Table B1. A more detailed description of velocity and vorticity budget diagnostic calculations in MOM6 is available at Khatri et al. (2023).

B1 Remapping contribution

In GFDL-MOM6, vertically-integrated zonal and meridional velocity budgets can be diagnosed according to

$$\begin{aligned} D \times \texttt{hf\_dudt\_2d} \;\; = \;\; & \texttt{intz\_CAu\_2d} + \texttt{intz\_PFu\_2d} + \texttt{intz\_u\_BT\_accel\_2d} \\ & + \texttt{intz\_diffu\_2d} + \frac{\texttt{taux}}{\rho_o} - \frac{\texttt{taux\_bot}}{\rho_o} + \texttt{remapping(u)}, \end{aligned} \tag{B1}$$

Term	Relevant Diagnostic Calculations
V	$\texttt{vmo\_2d}/(\rho_o \Delta x)$, where Δx is the zonal grid spacing and $\rho_o = 1035$ kg m^{-3}
$J(p_{\mathrm{b}}, H)$	see section B2
$\hat{\boldsymbol{z}} \cdot (\nabla \wedge \boldsymbol{\tau}_{\mathrm{s}})$	$\partial_x\,[\texttt{tauy}] - \partial_y\,[\texttt{taux}]$
$\hat{\boldsymbol{z}} \cdot (\nabla \wedge \boldsymbol{\tau}_{\mathrm{b}})$	$\partial_x\,[\texttt{tauy\_bot}] - \partial_y\,[\texttt{taux\_bot}]$
$\hat{\boldsymbol{z}} \cdot (\nabla \wedge \mathcal{A})$	$\partial_x\,[\texttt{intz\_rvxu\_2d} + \texttt{intz\_gKEv\_2d}] - \partial_y\,[\texttt{intz\_rvxv\_2d} + \texttt{intz\_gKEu\_2d}]$ + vertical remap contribution
$\hat{\boldsymbol{z}} \cdot (\nabla \wedge \mathcal{B})$	$\partial_x\,[\texttt{intz\_diffv\_2d}] - \partial_y\,[\texttt{intz\_diffu\_2d}]$
Q_m	wfo or PRCmE
$\partial_t \eta$	$\texttt{wfo}/\rho_o - \partial_x\,[\texttt{umo\_2d}/(\rho_o \Delta y)] - \partial_y\,[\texttt{vmo\_2d}/(\rho_o \Delta x)]$ (following equation (A16))
$\hat{\boldsymbol{z}} \cdot (\nabla \wedge \mathcal{U}_t)$	$\partial_x\,[D \times \texttt{hf\_dvdt\_2d}] - \partial_y\,[D \times \texttt{hf\_dudt\_2d}]$

Table B1. Method for the computations of vorticity budget terms using depth-integrated momentum budget diagnostics ($D = H + \eta$ is the full depth of the ocean) in MOM6. The contribution from remapping in $\nabla \wedge \mathcal{A}$ can be computed as discussed in section B1. 'intz' and '2d' in diagnostic names indicate vertical-integral; for example, intz_diffv_2d is the vertical-integral of diffv diagnostic. Note that hf_dvdt_2d and hf_dudt_2d are the depth-averaged velocity-tendency diagnostics, thus requiring multiplication by the ocean depth, D, in $\nabla \wedge \mathcal{U}_t$ calculation.

$$
\begin{aligned}
D \times \texttt{hf\_dvdt\_2d} \quad &= \quad \texttt{intz\_CAv\_2d} + \texttt{intz\_PFv\_2d} + \texttt{intz\_v\_BT\_accel\_2d} \\
&\quad + \texttt{intz\_diffv\_2d} + \frac{\texttt{tauy}}{\rho_o} - \frac{\texttt{tauy\_bot}}{\rho_o} + \texttt{remapping(v)}. \qquad \text{(B2)}
\end{aligned}
$$

Except for the last term on the RHS in equations (B1-B2), the rest of the terms are names of the MOM6 diagnostics corresponding to vertical-integrals of terms in equation (A1). hf_dudt_2d and hf_dvdt_2d are the depth-averaged velocity-tendency diagnostics, intz_CAu_2d and intz_CAv_2d are the diagnostics for the vertical-integral of $(f+\zeta)\hat{\boldsymbol{z}}\wedge\mathbf{u}+\nabla K$, intz_PFu_2d + intz_u_BT_accel_2d and intz_PFv_2d + intz_v_BT_accel_2d are the diagnostics for the vertical-integral of $\nabla p/\rho_o$, intz_diffu_2d is the diagnostic for the vertical-integral of $\mathcal{F}^{(\text{horz diff})}$, taux and tauy are the surface wind stress diagnostics, and taux_bot and tauy_bot are the bottom friction diagnostics. The remapping terms correspond to $w^{(\dot{r})}\,\partial_z \mathbf{u}$, which are not available to be saved as online diagnostics in the currrent version of MOM6. Thus, the remapping terms are diagnosed offline as a residual in the velocity budget equations (B1-B2). Refer to the online documentation, mom6-analysiscookbook.readthedocs.io/en/latest/notebooks/Closing_momentum_budget.html, for full details of momentum diagnostics in MOM6 model.

To compute the contribution of the remapping terms in the vorticity budget, we calculate the curl of the depth-integrated remapping terms diagnosed as residuals from the depth-integrated velocity budget diagnostics. We found that the contribution of the remapping term to the barotropic vorticity budget is minimal, and the vorticity budget closes well even without accounting for the remapping term. This result suggests that the remapping term is not a significant factor in the present analyses.

B2 Bottom pressure torque calculation

From the development in equations (A14-A16), we are required to use the following identity to derive the barotropic vorticity equation (A17).

$$\hat{\boldsymbol{z}} \cdot \left(\nabla \wedge \left[f \hat{\mathbf{z}} \wedge \int_{-H}^{\eta} \mathbf{u}\, \mathrm{d}z \right] \right) = \beta\, V + f \frac{Q_m}{\rho_o} - f \partial_t \eta. \tag{B3}$$

Generally, the expression on the LHS in equation (B3) results in significant cancellation between the zonal and meridional gradients in the curl operation and the small residual is equal to $\beta\, V$ (plus small contributions from nonzero Q_m and $\partial_t \eta$). However, the analytical result in equation (B3) need not hold in an ocean model, which solves for velocity on a discretized grid. On the MOM6 native grid, cancellation between the zonal and meridional gradients in $\nabla \wedge \left[f \hat{\mathbf{z}} \wedge \int_{-H}^{\eta} \mathbf{u}\, \mathrm{d}z \right]$ does not occur as expected and the residual, which is due to numerical errors, is at least two orders of magnitudes larger than $\beta\, V + f \frac{Q_m}{\rho_o} - f \partial_t \eta$ (see Figures B1a-B1c).

These numerical errors can lead to spurious forces in vorticity balances and corrupt bottom pressure torques (Styles et al., 2022). These spurious signals arise due to the handling of the Coriolis acceleration and the representation of bathymetry in energy and enstrophy conserving schemes on a discrete C-grid (Arakawa & Lamb, 1981). As a result, a C-grid model does not satisfy discrete versions of the Leibniz's rule, which is used in equation (A13), leading to spurious forces in vorticity balances. MOM6 is discretized using a C-grid and employs a vertical Lagrangian-remap method on a hybrid z^*-isopycnal vertical coordinate to simulate the ocean state (Adcroft et al., 2019; Griffies et al., 2020). Hence, bottom pressure torque diagnosed in MOM6 is expected to suffer from these spurious forces (Waldman & Giordani, 2023; Styles et al., 2022). To diagnose physically relevant signals in bottom pressure torque, we need to account for these numerical errors. In some cases, it may be possible to disentangle physical and spurious contributions to vorticity budget terms offline from the knowledge of horizontal velocities and the model grid scale factors in C-grid models. For example, Waldman and Giordani (2023) proposed a method for diagnosing vorticity budget terms in NEMO ocean model; however, the method does not resolve all numerical issues.

In the present study, we take an alternative approach by making use of the terms leading to a closed momentum budget at every grid point. Thus, if we compute the curls of depth-integrated velocity budget diagnostics, the resultant vorticity budget also closes at every grid point. This closure implies that the sum of numerical errors present in individual vorticity budget terms, diagnosed using the discrete curl operations, must vanish at every grid point. Similar to numerical errors in $\nabla\wedge\left[f\hat{\mathbf{z}}\wedge\int_{-H}^{\eta}\mathbf{u}\,\mathrm{d}z\right]$, we observe unrealistic large signals in $-\nabla\wedge\left[\frac{1}{\rho_o}\int_{-H}^{\eta}\nabla p\,\mathrm{d}z\right]$ (Figure B1d). We hypothesize that these large signals are mostly numerical errors due to discretization. Fortunately, the Coriolis acceleration and pressure gradient acceleration are discretized in a consistent manner, so that numerical errors in their curls are roughly equal in magnitude and largely cancel (see Figures B1a, B1d, B1e).

We make an assumption that spurious signals are only present separately in the curls of depth-integrated Coriolis acceleration and pressure gradient terms. To obtain physically realistic magnitudes and spatial structure of bottom pressure torque, we then use the following equation

$$\frac{J(p_\mathrm{b},H)}{\rho_o} = \hat{\boldsymbol{z}}\cdot\left(-\nabla\wedge\left[\frac{1}{\rho_o}\int_{-H}^{\eta}\nabla p\,\mathrm{d}z\right]\right)+\hat{\boldsymbol{z}}\cdot\left(-\nabla\wedge\left[f\hat{\mathbf{z}}\wedge\int_{-H}^{\eta}\mathbf{u}\,\mathrm{d}z\right]\right)+\beta\,V+f\,\frac{Q_m}{\rho_o}-f\,\partial_t\eta, \tag{B4}$$

which leads to the following diagnostic equation (see equations (B1-B2) for the description of diagnostics)

$$\begin{aligned}\frac{J(p_\mathrm{b},H)}{\rho_o} &= \partial_x\left[\texttt{intz\_PFv\_2d}+\texttt{intz\_v\_BT\_accel\_2d}\right]-\partial_y\left[\texttt{intz\_PFu\_2d}+\texttt{intz\_u\_BT\_accel\_2d}\right]\\ &+ \partial_x\left[\texttt{intz\_CAv\_2d}-\texttt{intz\_rvxu\_2d}-\texttt{intz\_gKEv\_2d}\right]\\ &- \partial_y\left[\texttt{intz\_CAu\_2d}-\texttt{intz\_rvxv\_2d}-\texttt{intz\_gKEu\_2d}\right]\\ &+ \frac{\beta}{\rho_o\Delta x}\times\texttt{vmo\_2d}+\frac{f}{\rho_o}\times\texttt{wfo}-f\partial_t\eta.\end{aligned} \tag{B5}$$

Since the sum of the last four terms on the RHS in equation (B4) vanishes (see equation B3), the analytical expression (B4) computes the curl of the depth-integrated pressure gradient terms, which is bottom pressure torque. By using the diagnostic approach of equation (B5), we eliminate the spurious signals in bottom pressure torque because numerical errors in the first two terms on the RHS in equation (B5) cancel out.

The spatial structure and magnitudes of diagnosed bottom pressure torque (Figure B1f) agree well with results from Le Corre et al. (2020) (see their Figure 7b), who used a terrain following vertical coordinate C-grid model (which is partially immune to the numerical issues identified by Styles et al. (2022) and Waldman and Giordani (2023)). Furthermore, there is a fair consistency between the present results and bottom pressure torque diagnosed using B-grid model outputs (Hughes & De Cuevas, 2001; Yeager, 2015), which also do not suffer from numerical issues present in C-grid models (Styles et al., 2022).

Our diagnostic approach assumes that numerical errors in $-\nabla\wedge\left[f\hat{\mathbf{z}}\wedge\int_{-H}^{\eta}\mathbf{u}\,\mathrm{d}z\right]$ and $-\nabla\wedge\left[\frac{1}{\rho_o}\int_{-H}^{\eta}\nabla p\,\mathrm{d}z\right]$ are exactly equal in magnitude and opposite in sign, which need not be true in general. Numerical errors may also be present in nonlinear advection, bottom stress, and horizontal friction in the barotropic vorticity budget. However, accelerations from the pressure gradient and Coriolis appearing in the velocity equation are at least two orders of magnitude larger than the rest of the terms (Figure B2). Therefore, it is safe to assume that numerical errors are contained in pressure gradient and Coriolis acceleration, with the diagnostic approach of equation (B5) being a practical diagnostic method.

Appendix C Coarse-graining and Vorticity Budget Magnitudes

To assess the impact of coarse-graining on the actual magnitudes of vorticity budget terms, the zonally-averaged profiles of $\{|F_\ell|\}$ are examined. As seen in Figure C1, the zonal-mean absolute values of the vorticity budget terms are largest in the Southern Ocean (between 40°S and 60°S) followed by oceanic regions at 50°N–70°N latitude bands. $\{|F_\ell|\}$ values of coarse-grained fields for 200 km coarse-graining scale are five-ten times larger than $\{|F_\ell|\}$ values for 1000 km coarse-graining scale. In the zonal average, βV, bottom pressure torque, and nonlinear advection term are of the largest magnitudes.

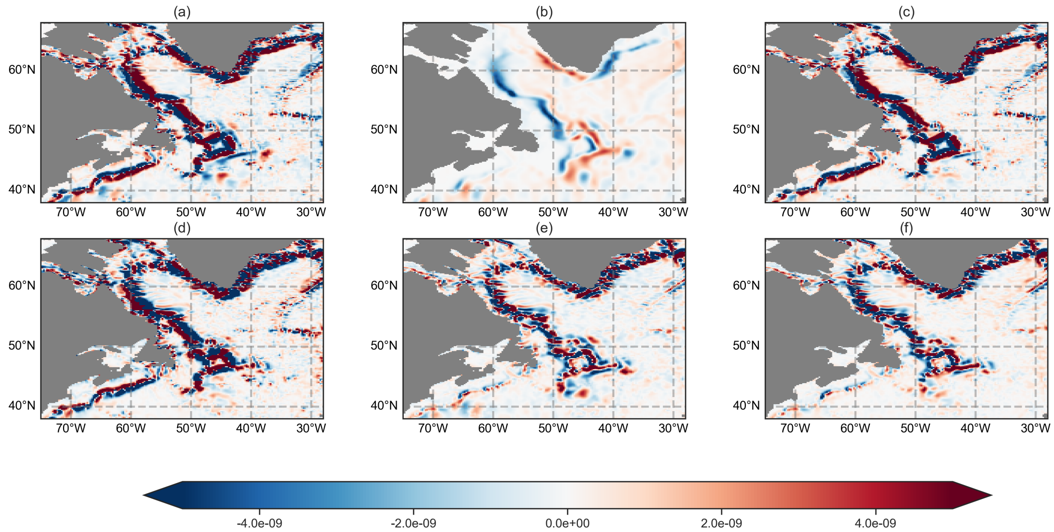

Figure B1. Time-mean (1958–2017) of (a) Vertical component of the curl of depth-integrated planetary vorticity advection, $-\nabla \wedge \left[f\hat{\mathbf{z}} \wedge \int_{-H}^{\eta} \mathbf{u}\,\mathrm{d}z\right]$, in model diagnostics (terms in second and third lines on the RHS in equation B5) (b) $\beta V + f\,Q_m/\rho_o - f\partial_t\eta$ (c) sum of fields shown in panels a and b (d) Vertical component of the the curl of depth-integrated pressure gradient, $-\nabla \wedge \left[\frac{1}{\rho_o}\int_{-H}^{\eta} \nabla p\,\mathrm{d}z\right]$, in model diagnostics (terms in the first line on the RHS in equation B5) (e) sum of fields shown in panels a and d (f) sum of fields shown in panels c and d to compute bottom pressure torque. No coarse-graining (or regridding) was applied and the plotted diagnostics are on the model native grid (units are in m s^{-2}). However, for a better visualization, plotted diagnostics were smoothed by averaging over neighboring four grid points to remove grid-scale noise (used GCM-Filters package Loose et al., 2022).

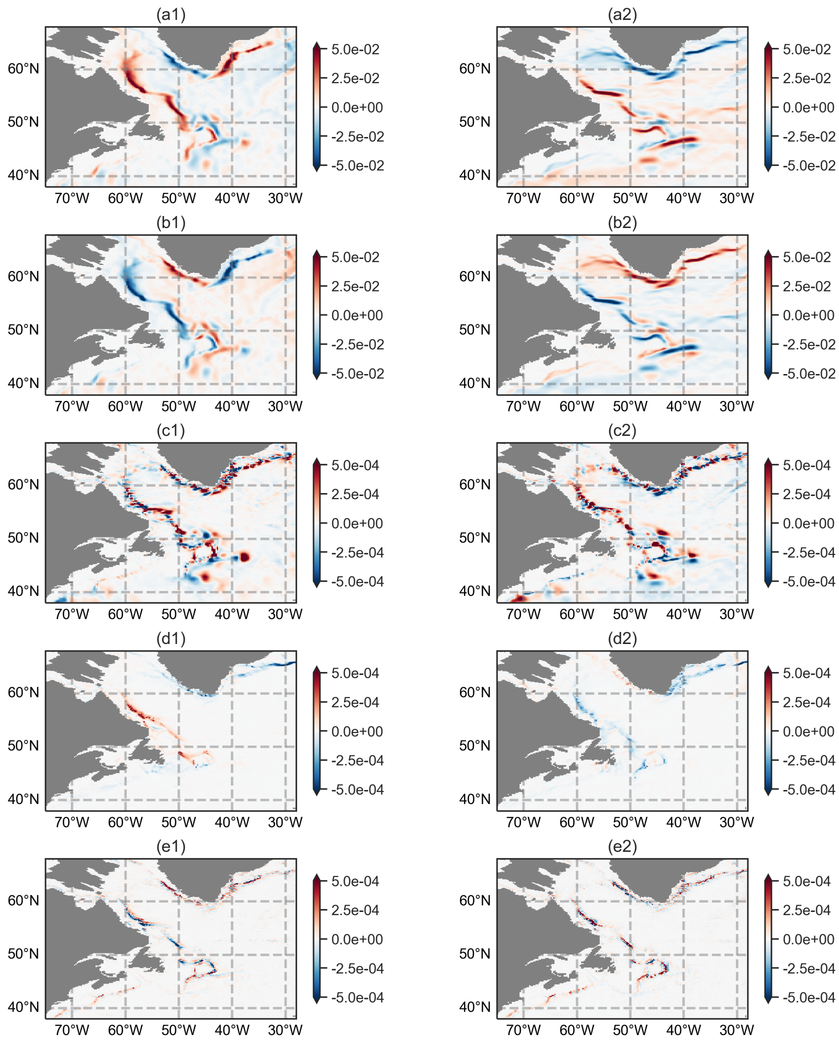

Figure B2. Time-mean (1958–2017) model diagnostics for (a) Depth-integrated pressure gradient term, $-\frac{1}{\rho_o}\int_{-H}^{\eta} \nabla p \, \mathrm{d}z$, (b) Depth-integrated Coriolis advection, $-f\hat{\mathbf{z}} \wedge \int_{-H}^{\eta} \mathbf{u} \, \mathrm{d}z$, (c) Depth-integrated nonlienar advection, $\mathcal{A}$, (d) Bottom friction term, $-\boldsymbol{\tau}_{\mathrm{b}}/\rho_o$, (e) Depth-integrated horizontal diffusion term, $\mathcal{B}$. Left and right panels are for the zonal and meridional velocity diagnostics (units are in $\mathrm{m}^2\ \mathrm{s}^{-2}$), respectively.

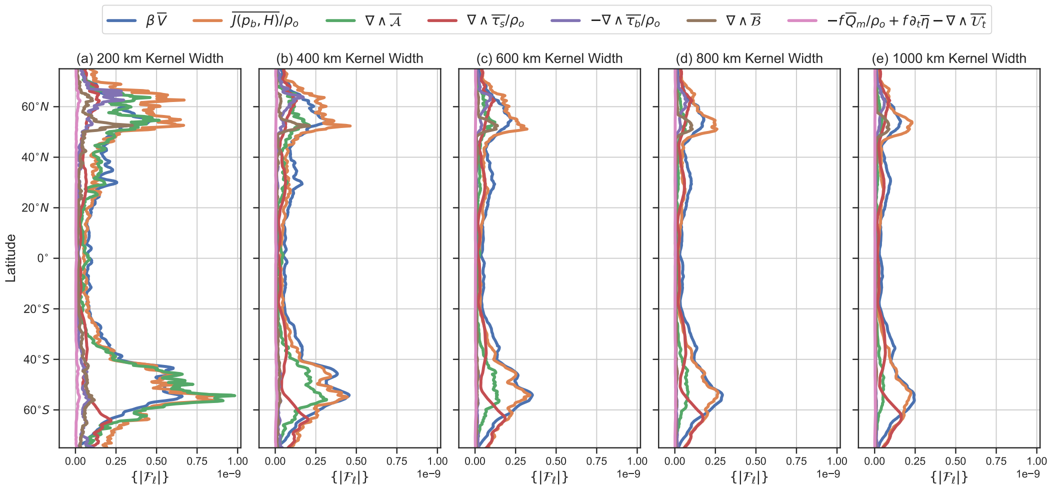

Figure C1. Latitude vs zonal-mean absolute vorticity budget magnitudes, $\{|F_\ell|\}$ (units are in m s^{-2}), of vorticity budget terms as a function of coarse-graining scale. Note that $\hat{\boldsymbol{z}}\cdot$ is omitted in the legends.

With increasing coarse-graining scale, the nonlinear advection term becomes much smaller and βV is mainly balanced by bottom pressure torque.

Appendix D Sensitivity of Vorticity Balances to the Filtering Method

To test the dependence of vorticity balances on the shape of filter kernel and filtering algorithm, we spatially filter the vorticity budget terms with a Gaussian kernel using GCM-Filters package (Loose et al., 2022), which employs a diffusion-based filtering scheme (Grooms et al., 2021), and repeat the analysis shown in section 3.1. In contrast to the fixed-kernel approach that we used in coarse-graining, GCM-Filters modifies the shape of the Gaussian kernel near land-sea boundaries (Grooms et al., 2021). Nevertheless, the spatial maps of filtered vorticity terms in Figure D1 look similar to maps shown in Figure 3 and the overall conclusions about vorticity balances remain the same.

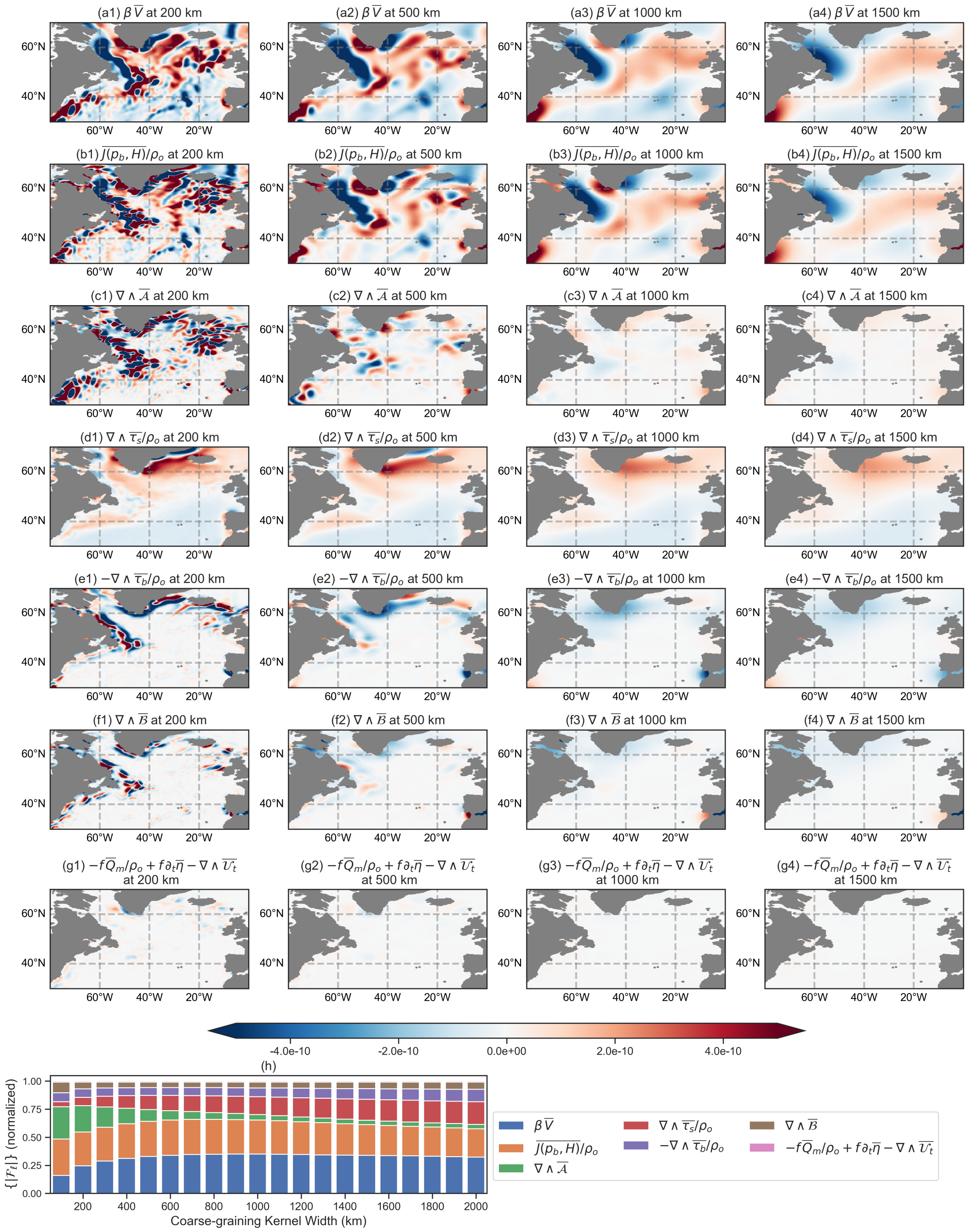

Figure D1. Vorticity budget analysis for the North Atlantic Ocean (a-g) Time-mean (1958–2017, indicated with overbars) spatial maps of filtered barotropic vorticity budget terms (used GCM-Filters package, units are in m s^{-2}) as a function of filter scale; (h) Normalized magnitudes of the absolute budget terms (see equation 6) at different filter scales (in degree). $\{|F_\ell|\}$ is computed for the region bounded between 30°N–70°N and 80°W–0°W. Note that $\hat{\boldsymbol{z}}\cdot$ is omitted in panel titles and legends.

Acknowledgments

We thank Andrew Kiss and an anonymous reviewer for their thorough and insightful comments that greatly enhanced the clarity of this paper. We are grateful to Alistair Adcroft and Robert Hallberg for help with the implementation of depth-integrated momentum budget diagnostics in MOM6. Discussions with Chris Hughes were very helpful in this work, and we thank Graeme MacGilchrist and Wenda Zhang for comments on a draft of this manuscript. HK acknowledges the support from National Oceanic and Atmospheric Administration (NOAA) grant NA18OAR4320123 and Natural Environment Research Council (NERC) grant NE/T013494/1. MB acknowledges the support from the European Research Council (ERC) under the European Union's Horizon 2020 research and innovation programme (Grant Agreement No. 882340). HA and BS acknowledge support from US NASA grant 80NSSC18K0772 and US NSF grants OCE-2123496, PHY-2020249.

Open Research

FlowSieve filtering package (Storer & Aluie, 2023) used in the analysis of this paper is available at `https://github.com/husseinaluie/FlowSieve`. Post-processed data and Python scripts used to produce the figures are available at Khatri et al. (2023) and `https://github.com/hmkhatri/Barotropic_Vorticity_Analysis_GCM`.

References

Adcroft, A., Anderson, W., Balaji, V., Blanton, C., Bushuk, M., Dufour, C. O., ... others (2019). The GFDL global ocean and sea ice model OM4.0: Model description and simulation features. *Journal of Advances in Modeling Earth Systems*, *11*(10), 3167–3211. doi: 10.1029/2019MS001726

Aluie, H. (2019). Convolutions on the sphere: Commutation with differential operators. *GEM-International Journal on Geomathematics*, *10*(1), 1–31. doi: 10.1007/s13137-019-0123-9

Aluie, H., Hecht, M., & Vallis, G. K. (2018). Mapping the energy cascade in the North Atlantic Ocean: The coarse-graining approach. *Journal of Physical Oceanography*, *48*(2), 225–244. doi: 10.1175/JPO-D-17-0100.1

Arakawa, A., & Lamb, V. R. (1981). A potential enstrophy and energy conserving scheme for the shallow water equations. *Monthly Weather Review*, *109*(1), 18–

36. doi: 10.1175/1520-0493(1981)109⟨0018:APEAEC⟩2.0.CO;2

Bell, M. J. (1999). Vortex stretching and bottom torques in the bryan-cox ocean circulation model. *Journal of Geophysical Research: Oceans*, *104* (C10), 23545–23563. doi: 10.1029/1999JC900064

Buzzicotti, M., Storer, B. A., Khatri, H., Griffies, S. M., & Aluie, H. (2023). Spatio-temporal coarse-graining decomposition of the global ocean geostrophic kinetic energy. *Journal of Advances in Modeling Earth Systems*, *15* (6), e2023MS003693. doi: 10.1029/2023MS003693

Chelton, D. B., Schlax, M. G., & Samelson, R. M. (2011). Global observations of nonlinear mesoscale eddies. *Progress in Oceanography*, *91* (2), 167–216. doi: 10.1016/j.pocean.2011.01.002

Chelton, D. B., Schlax, M. G., Samelson, R. M., & de Szoeke, R. A. (2007). Global observations of large oceanic eddies. *Geophysical Research Letters*, *34* (15). doi: 10.1029/2007GL030812

Eden, C. (2007). Eddy length scales in the North Atlantic Ocean. *Journal of Geophysical Research: Oceans*, *112* (C6). doi: 10.1029/2006JC003901

Fofonoff, N. P. (1955). Steady flow in a frictionless homogeneous ocean. *Journal of Marine Research*, *13* (3).

Gray, A. R., & Riser, S. C. (2014). A global analysis of Sverdrup balance using absolute geostrophic velocities from Argo. *Journal of Physical Oceanography*, *44* (4), 1213–1229. doi: 10.1175/JPO-D-12-0206.1

Griffies, S. M., Adcroft, A., & Hallberg, R. W. (2020). A primer on the vertical Lagrangian-remap method in ocean models based on finite volume generalized vertical coordinates. *Journal of Advances in Modeling Earth Systems*, *12* (10), e2019MS001954. doi: 10.1029/2019MS001954

Griffies, S. M., Danabasoglu, G., Durack, P. J., Adcroft, A. J., Balaji, V., Böning, C. W., ... Yeager, S. (2016). OMIP contribution to CMIP6: Experimental and diagnostic protocol for the physical component of the Ocean Model Intercomparison Project. *Geoscientific Model Development*, *9*, 3231–3296. doi: 10.5194/gmd-9-3231-2016

Griffies, S. M., & Hallberg, R. W. (2000). Biharmonic friction with a smagorinsky-like viscosity for use in large-scale eddy-permitting ocean models. *Monthly Weather Review*, *128* (8), 2935–2946. doi: 10.1175/1520-0493(2000)128⟨2935:

BFWASL⟩2.0.CO;2

Grooms, I., Loose, N., Abernathey, R., Steinberg, J., Bachman, S. D., Marques, G., … Yankovsky, E. (2021). Diffusion-based smoothers for spatial filtering of gridded geophysical data. *Journal of Advances in Modeling Earth Systems*, *13*(9), e2021MS002552. doi: 10.1029/2021MS002552

Gula, J., Molemaker, M. J., & McWilliams, J. C. (2015). Gulf Stream dynamics along the southeastern US seaboard. *Journal of Physical Oceanography*, *45*(3), 690–715. doi: 10.1175/JPO-D-14-0154.1

Haidvogel, D. B., McWilliams, J. C., & Gent, P. R. (1992). Boundary current separation in a quasigeostrophic, eddy-resolving ocean circulation model. *Journal of Physical Oceanography*, *22*(8), 882–902. doi: 10.1175/1520-0485(1992)022⟨0882:BCSIAQ⟩2.0.CO;2

Holland, W. R. (1967). On the wind-driven circulation in an ocean with bottom topography. *Tellus*, *19*(4), 582–600. doi: 10.3402/tellusa.v19i4.9825

Holland, W. R. (1973). Baroclinic and topographic influences on the transport in western boundary currents. *Geophysical Fluid Dynamics*, *4*(3), 187–210. doi: 10.1080/03091927208236095

Hughes, C. W. (2000). A theoretical reason to expect inviscid western boundary currents in realistic oceans. *Ocean Modelling*, *2*(1-2), 73–83. doi: 10.1016/S1463-5003(00)00011-1

Hughes, C. W. (2005). Nonlinear vorticity balance of the Antarctic Circumpolar Current. *Journal of Geophysical Research: Oceans*, *110*(C11). doi: 10.1029/2004JC002753

Hughes, C. W., & De Cuevas, B. A. (2001). Why western boundary currents in realistic oceans are inviscid: A link between form stress and bottom pressure torques. *Journal of Physical Oceanography*, *31*(10), 2871–2885. doi: 10.1175/1520-0485(2001)031⟨2871:WWBCIR⟩2.0.CO;2

Ierley, G. R., & Sheremet, V. A. (1995). Multiple solutions and advection-dominated flows in the wind-driven circulation. part i: Slip. *Journal of Marine Research*, *53*(5), 703–737.

Jackson, L., Hughes, C. W., & Williams, R. G. (2006). Topographic control of basin and channel flows: The role of bottom pressure torques and friction. *Journal of Physical Oceanography*, *36*(9), 1786–1805. doi: 10.1175/JPO2936.1

Khatri, H., Griffies, S. M., Storer, B. A., Buzzicotti, M., Aluie, H., Sonnewald, M., ... Shao, A. (2023). *Barotropic vorticity budget analysis in a global ocean simulation.* Zenodo. doi: 10.5281/zenodo.7920588

Kiss, A. E. (2002). Potential vorticity "crises", adverse pressure gradients, and western boundary current separation. *Journal of Marine Research*, *60*(6), 779–803.

Kiss, A. E. (2004). Potential vorticity dynamics in a domain with closed geostrophic contours. i: Steady linear flows. *Journal of Marine Research*, *62*(4), 461–489.

Le Bras, I. A.-A., Sonnewald, M., & Toole, J. M. (2019). A barotropic vorticity budget for the subtropical North Atlantic based on observations. *Journal of Physical Oceanography*, *49*(11), 2781–2797. doi: 10.1175/JPO-D-19-0111.1

Le Corre, M., Gula, J., & Treguier, A.-M. (2020). Barotropic vorticity balance of the North Atlantic subpolar gyre in an eddy-resolving model. *Ocean Science*, *16*(2), 451–468. doi: 10.5194/os-16-451-2020

Loose, N., Abernathey, R., Grooms, I., Busecke, J., Guillaumin, A., Yankovsky, E., ... others (2022). GCM-Filters: A python package for diffusion-based spatial filtering of gridded data. *Journal of Open Source Software*, *7*(70), 3947. doi: 10.21105/joss.03947

Lu, Y., & Stammer, D. (2004). Vorticity balance in coarse-resolution global ocean simulations. *Journal of Physical Oceanography*, *34*(3), 605–622. doi: 10.1175/2504.1

Mertz, G., & Wright, D. G. (1992). Interpretations of the JEBAR term. *Journal of Physical Oceanography*, *22*(3), 301–305. doi: 10.1175/1520-0485(1992)022⟨0301:IOTJT⟩2.0.CO;2

Munk, W. H. (1950). On the wind-driven ocean circulation. *Journal of Atmospheric Sciences*, *7*(2), 80–93. doi: 10.1175/1520-0469(1950)007⟨0080:OTWDOC⟩2.0.CO;2

Neme, J., England, M. H., Hogg, A. M., Khatri, H., & Griffies, S. M. (2023). The role of bottom friction in mediating the response of the weddell gyre circulation to changes in surface stress and buoyancy fluxes. *ESS Open Archive*. doi: 10.22541/essoar.169228895.55803191/v1

Palóczy, A., McClean, J. L., Gille, S. T., & Wang, H. (2020). The large-scale vorticity balance of the Antarctic continental margin in a fine-resolution global simulation. *Journal of Physical Oceanography*, *50*(8), 2173–2188. doi: 10.1175/JPO-D-19-0307.1

Pedlosky, J. (1987). *Geophysical fluid dynamics.* Springer New York, NY. doi: 10.1007/978-1-4612-4650-3

Rai, S., Hecht, M., Maltrud, M., & Aluie, H. (2021). Scale of oceanic eddy killing by wind from global satellite observations. *Science Advances*, *7*(28), eabf4920. doi: 10.1126/sciadv.abf4920

Rhines, P. B. (1975). Waves and turbulence on a beta-plane. *Journal of Fluid Mechanics*, *69*(3), 417–443. doi: 10.1017/S0022112075001504

Rintoul, S. R. (2018). The global influence of localized dynamics in the Southern Ocean. *Nature*, *558*, 209–218. doi: 10.1038/s41586-018-0182-3

Rintoul, S. R., Hughes, C. W., & Olbers, D. (2001). The Antarctic circumpolar current system. In *International Geophysics* (Vol. 77, pp. 271–XXXVI). Elsevier. doi: 10.1016/S0074-6142(01)80124-8

Rintoul, S. R., & Naveira Garabato, A. C. (2013). Dynamics of the Southern Ocean circulation. In G. Siedler, S. M. Griffies, J. Gould, & J. Church (Eds.), *Ocean circulation and climate, 2nd edition: A 21st century perspective* (Vol. 103, pp. 471–492). Academic Press.

Schoonover, J., Dewar, W., Wienders, N., Gula, J., McWilliams, J. C., Molemaker, M. J., … Yeager, S. (2016). North atlantic barotropic vorticity balances in numerical models. *Journal of Physical Oceanography*, *46*(1), 289–303. doi: 10.1175/JPO-D-15-0133.1

Sonnewald, M., & Lguensat, R. (2021). Revealing the impact of global heating on North Atlantic circulation using transparent machine learning. *Journal of Advances in Modeling Earth Systems*, *13*(8), e2021MS002496. doi: 10.1029/2021MS002496

Sonnewald, M., Reeve, K. A., & Lguensat, R. (2023). A southern ocean supergyre as a unifying dynamical framework identified by physics-informed machine learning. *Communications Earth & Environment*, *4*(1), 153. doi: 10.1038/s43247-023-00793-7

Sonnewald, M., Wunsch, C., & Heimbach, P. (2019). Unsupervised learning reveals geography of global ocean dynamical regions. *Earth and Space Science*, *6*(5), 784–794. doi: 10.1029/2018EA000519

Stewart, A. L., McWilliams, J. C., & Solodoch, A. (2021). On the role of bottom pressure torques in wind-driven gyres. *Journal of Physical Oceanography*, *51*(5), 1441–1464. doi: 10.1175/JPO-D-20-0147.1

Stommel, H. (1948). The westward intensification of wind-driven ocean currents. *EOS, Transactions American Geophysical Union*, *29*(2), 202–206. doi: 10.1029/TR029i002p00202

Storer, B. A., & Aluie, H. (2023). FlowSieve: A Coarse-Graining utility for geophysical flows on the sphere. *Journal of Open Source Software*, *8*(84), 4277. Retrieved from `https://doi.org/10.21105/joss.04277` doi: 10.21105/joss.04277

Storer, B. A., Buzzicotti, M., Khatri, H., Griffies, S. M., & Aluie, H. (2022). Global energy spectrum of the general oceanic circulation. *Nature Communications*, *13*(1), 1–9. doi: 10.1038/s41467-022-33031-3

Styles, A. F., Bell, M. J., Marshall, D. P., & Storkey, D. (2022). Spurious forces can dominate the vorticity budget of ocean gyres on the c-grid. *Journal of Advances in Modeling Earth Systems*, e2021MS002884. doi: 10.1029/2021MS002884

Sverdrup, H. U. (1947). Wind-driven currents in a baroclinic ocean; with application to the equatorial currents of the eastern pacific. *Proceedings of the National Academy of Sciences*, *33*(11), 318–326. doi: 10.1073/pnas.33.11.318

Thomas, M. D., De Boer, A. M., Johnson, H. L., & Stevens, D. P. (2014). Spatial and temporal scales of Sverdrup balance. *Journal of Physical Oceanography*, *44*(10), 2644–2660. doi: 10.1175/JPO-D-13-0192.1

Tsujino, H., Urakawa, S., Griffies, S. M., Danabasoglu, G., Adcroft, A. J., Amaral, A. E., ... Yu, Z. (2020). Evaluation of global ocean-sea-ice model simulations based on the experimental protocols of the Ocean Model Intercomparison Project phase 2 (OMIP-2). *Geoscientific Model Development*, *13*, 3643–3708. doi: 10.5194/gmd-13-3643-2020

Tsujino, H., Urakawa, S., Nakano, H., Small, R., Kim, W., Yeager, S., ... Yamazaki, D. (2018). JRA-55 based surface dataset for driving ocean-sea-ice models (JRA55-do). *Ocean Modelling*, *130*, 79–139. doi: 10.1016/j.ocemod.2018.07.002

Waldman, R., & Giordani, H. (2023). Ocean barotropic vorticity balances: theory and application to numerical models. *Journal of Advances in Modeling Earth Systems*, *15*(4), e2022MS003276. doi: 10.1029/2022MS003276

Welander, P. (1968). Wind-driven circulation in one-and two-layer oceans of variable depth. *Tellus*, *20*(1), 1–16. doi: 10.1111/j.2153-3490.1968.tb00347.x

Wunsch, C. (2011). The decadal mean ocean circulation and Sverdrup balance. *Journal of Marine Research*, *69*(2-3), 417–434.

Yeager, S. (2015). Topographic coupling of the Atlantic overturning and gyre circulations. *Journal of Physical Oceanography*, *45*(5), 1258–1284. doi: 10.1175/JPO-D-14-0100.1

Zhang, R., & Vallis, G. K. (2007). The role of bottom vortex stretching on the path of the north atlantic western boundary current and on the northern recirculation gyre. *Journal of Physical Oceanography*, *37*(8), 2053–2080. doi: 10.1175/JPO3102.1